

Journal of Statistical Physics manuscript No.
 (will be inserted by the editor)

An in-depth view of the microscopic dynamics of Ising spin glasses at fixed temperature

F. Belletti · A. Cruz · L.A. Fernandez ·
 A. Gordillo-Guerrero · M. Guidetti · A. Maiorano ·
 F. Mantovani · E. Marinari · V. Martin-Mayor ·
 J. Monforte · A. Muñoz Sudupe · D. Navarro ·
 G. Parisi · S. Perez-Gaviro · J.J. Ruiz-Lorenzo ·
 S.F. Schifano · D. Sciretti · A. Tarancón ·
 R. Tripiccione · D. Yllanes

the date of receipt and acceptance should be inserted later

Abstract Using the dedicated computer Janus, we follow the nonequilibrium dynamics of the Ising spin glass in three dimensions for eleven orders of magnitude. The use of integral estimators for the coherence and correlation lengths allows us to study dynamic heterogeneities and the presence of a replicon mode and to obtain safe bounds on the Edwards-Anderson order parameter below the critical temperature. We obtain good agreement with experimental determinations of the temperature-dependent decay exponents for the thermoremanent magnetization. This magnitude is observed to scale with the much harder to measure coherence length, a potentially useful result for experimentalists. The exponents for energy relaxation display a linear dependence on temperature and reasonable extrapolations to the critical point. We conclude examining the time growth of the coherence length, with a comparison of critical and activated dynamics.

Keywords Spin glasses, nonequilibrium dynamics, characteristic length scales

F. Belletti · M. Guidetti · A. Maiorano · F. Mantovani · S.F. Schifano · R. Tripiccione
 Dipartimento di Fisica Università di Ferrara and INFN - Sezione di Ferrara, Ferrara, Italy.

A. Cruz · L.A. Fernandez · A. Gordillo-Guerrero · A. Maiorano · V. Martin-Mayor · J. Monforte · S. Perez-Gaviro · J.J. Ruiz-Lorenzo · D. Sciretti · A. Tarancón · D. Yllanes
 Instituto de Biocomputación y Física de Sistemas Complejos (BIFI), Zaragoza, Spain

A. Cruz · A. Tarancón
 Departamento de Física Teórica, Universidad de Zaragoza, 50009 Zaragoza, Spain.

L.A. Fernandez · V. Martin-Mayor · A. Muñoz Sudupe · D. Yllanes
 Departamento de Física Teórica I, Universidad Complutense, 28040 Madrid, Spain.

A. Gordillo-Guerrero
 Dpto. de Ingeniería Eléctrica, Electrónica y Automática, Universidad de Extremadura. Avda. de la Universidad s/n. 10071. Cáceres, Spain.

A. Maiorano · E. Marinari · G. Parisi · S. Perez-Gaviro
 Dipartimento di Fisica, SMC of INFM-CNR and INFN, Università di Roma *La Sapienza*, 00185 Roma, Italy.

D. Navarro
 Departamento de Ingeniería, Electrónica y Comunicaciones and Instituto de Investigación en Ingeniería de Aragón (I3A), Universidad de Zaragoza, 50018 Zaragoza, Spain.

J.J. Ruiz-Lorenzo
 Departamento de Física, Universidad de Extremadura, 06071 Badajoz, Spain.

1 Introduction

Below their glass temperature, Spin Glasses [1] (SG) are perennially out of equilibrium. The understanding of their sophisticated dynamical behavior is a long standing challenge both to theoretical and to experimental physics.

Aging [2] is a feature of SG dynamics that shows up even in the simplest experimental protocol, the *direct quench*. In these experiments, the SG is cooled as fast as possible to the working temperature below the critical one, $T < T_c$. It is then let to equilibrate for a *waiting time*, t_w , its properties to be probed at a later time, $t + t_w$. For instance one may cool the SG in the presence of an external field, which is switched off at time t_w . The so-called thermoremanent magnetization decays with time, but the larger t_w is, the slower the decay. In fact, it has been claimed that, if the cooling is fast enough, the thermoremanent magnetization depends upon t and t_w only through the combination t/t_w , at least for $10^{-3} < t/t_w < 10$ and t_w in the range $50\text{ s} - 10^4\text{ s}$ [3]. In other words, the only characteristic time scale is the sample's own age as a glass, t_w (this behavior is named Full Aging). Note, however, that there is some controversy regarding the natural time variable which could rather be t/t_w^μ with μ slightly less than one [4].

The time evolution is believed to be caused by the growth of coherent spatial domains. Great importance is ascribed to the size of these domains, the coherence length $\xi(t_w)$, which is accessible to experiments through estimates of Zeeman energies [5]. The time evolution of $\xi(t_w)$ plays a crucial role in the droplets theory of SG nonequilibrium isothermal dynamics [6]. Perhaps unsurprisingly, it also plays a central role in yet incipient attempts to rationalize memory and rejuvenation experiments (see [7, 8, 9, 10] and references therein), where the experimentalist probes the glassy state by playing with the working temperature.

Even for the simplest direct quench experiment, there is some polemics regarding the growth law of $\xi(t_w)$: some theories advocate a logarithmic growth [6], while a power law describes numerical simulations [11] or experiments [5] better (a somewhat intermediate scaling has been proposed by the Saclay group [12] and found useful in experimental work [8], see also Sect. 6 below). Nevertheless, two facts are firmly established: (i) the lower T is, the slower the growth of $\xi(t_w)$ and (ii) $\xi \sim 100$ lattice spacings, even for $T \sim T_c$ and t_w as large as 10^4 s [5]. Hence, the study of SG in thermal equilibrium seems confined to nanometric samples, or to numerical simulations.

There is clear evidence, both experimental [13] and theoretical [14, 15], for a thermodynamic origin of this sluggish dynamics. A SG phase appears below the critical temperature, T_c . Several theories propose mutually contradicting scenarios for the *equilibrium* SG phase: the droplets [16], replica symmetry breaking (RSB) [17], and the intermediate Trivial-Non-Trivial (TNT) picture [18]. Even if this equilibrium phase is experimentally unreachable (at least in human time scales), we now know [19] that it is nevertheless relevant to the nonequilibrium dynamics probed by experiments.

Droplets expects two equilibrium states related by global spin reversal. The SG order parameter, the spin overlap q (precise definitions are given below in Sect. 2), takes only two values $q = \pm q_{\text{EA}}$. In the RSB scenario an infinite number of pure states influence the dynamics [17, 20, 21], so that all $-q_{\text{EA}} \leq q \leq q_{\text{EA}}$ are reachable. TNT [18] describes the SG phase similarly to an antiferromagnet with random boundary conditions: even if q behaves as for RSB systems, TNT agrees with droplets in the vanishing surface to volume ratio of the largest thermally activated spin domains (i.e. the link-overlap defined below takes a single value).

Droplets' isothermal aging [6] is that of a disguised ferromagnet.¹ Indeed, superuniversality, the emerging picture of isothermal aging, has been found useful for the study of basically all coarsening systems. For $T < T_c$ the growing domains are compact geometrical objects. Even if the surface of these domains might be fractal, their surface to volume ratio vanishes as $\xi(t_w)$ diverges, see Eq. (13) below. Inside them, the spin overlap coherently takes one of its possible equilibrium values $q = \pm q_{\text{EA}}$. Time dependencies are entirely encoded in the growth law of these domains, since correlation functions (in principle depending on time and distance, r) are universal functions of $r/\xi(t_w)$.

We are not aware of any investigation of the dynamical consequences of the TNT picture. Nevertheless, the antiferromagnet analogy suggests that TNT systems will show coarsening behavior.

As for the RSB scenario, equilibrium states with a vanishing order parameter $q=0$ do exist. Hence, the nonequilibrium dynamics starts, and remains forever, with a vanishing order parameter. Furthermore, the replicon, a Goldstone mode analogous to magnons in Heisenberg ferromagnets, is present for all $T < T_c$ [22]. As a consequence, the spin overlap is expected to vanish *inside each domain* in the limit of a large $\xi(t_w)$. Furthermore, q is not a privileged observable (overlap equivalence [20]): the link overlap displays equivalent Aging behavior.

In order to be quantitative, these theoretical pictures of nonequilibrium dynamics need numerical computations for model systems. Indeed, several investigations have been carried out even for the simplest cooling protocol, the direct quench [9, 10, 11, 23, 24, 25, 26, 27, 28, 29]. A major drawback of this approach, however, is the shortness of the reachable times. Indeed, one Monte Carlo Step (MCS) corresponds to 10^{-12} s [1]. The experimental scale is at 10^{14} MCS (~ 100 s), while typical nonequilibrium simulations reach $\sim 10^{-5}$ s. The problem has been challenging enough to compel physicists to design high-performance computers for SG simulations [30, 31, 32].

The situation has dramatically changed thanks to *Janus* [32], an FPGA computer that allows us to simulate the dynamics of a reasonably large SG system for eleven orders of magnitude, from picoseconds to tenths of a second.² Thanks to Janus, we have recently performed a study of the nonequilibrium dynamics of the Ising Spin Glass [33]. We introduced novel analysis techniques that allow the computation of the coherence length in a model independent way. This was crucial to obtain evidence for a replicon correlator. Furthermore, we showed how to investigate overlap equivalence and presented evidence for it.

In this work, we shall concentrate on the simplest protocol, the direct quench, for an Ising SG. We present a detailed study of dynamic heterogeneities, an aspect untouched upon in [33] in spite of its relevance [27, 28, 29]. We show the first conclusive numerical evidence for a growing *correlation* length in the nonequilibrium dynamics, and its relationship with the *coherence* length $\xi(t_w)$ is explored. Furthermore, we compute the anomalous dimension for the two-time, two-site propagator (see definitions below). Due to their central role, a systematic way of extracting coherence (or correlation) lengths from numerical data is called for, but it has scarcely been investigated in the past (see however [10, 11, 23]). This is why we take here the occasion to give full details on our *integral* estimators [33] (see also [23]).

The layout of the rest of this paper is as follows. In Sect. 2 we define the model as well as the correlation functions and time sectors. We describe our simulations, which have been extended as compared with [33] and discuss the difficult topic of extracting the best

¹ However, when the temperature is varied, droplets theory predicts a more complex behavior for SGs than for ferromagnets, due to temperature chaos.

² The wall-clock time needed for this computation on a cubic lattice of 80 lattice spacings is some 25 days.

fit parameters from extremely correlated data. Sect. 3 is devoted to the integral estimators of the coherence (or correlation) lengths. To the best of our knowledge, the investigation of this technical (but crucial) issue was started in the context of lattice field theories [34]. These integral estimators were instrumental to develop modern Finite Size Scaling techniques for *equilibrium* critical phenomena [35, 36] and, therefore, to establish the existence of the Spin Glass phase in three dimensions [14, 15, 37]. In the context of nonequilibrium dynamics, new aspects (and opportunities) appear. In Sect. 4 we investigate the dynamic heterogeneities. In Sect. 5, the information gathered on length scales is used to analyze time correlation functions (and to extrapolate them to infinite time). We also study the thermoremanent magnetization. The crucial issue of the time growth of the coherence length $\xi(t_w)$ is considered in Sect. 6. We present our conclusions in Sect. 7

2 Model, correlation functions, time sectors

2.1 Model

The $D = 3$ Edwards-Anderson Hamiltonian is defined in terms of two types of degrees of freedom: dynamical and *quenched*. The dynamical ones are the Ising spins $\sigma_x = \pm 1$, which are placed on the nodes, x , of a cubic lattice of linear size L and periodic boundary conditions. The nondynamical (or quenched) ones are coupling constants assigned to the lattice links that join pairs of lattice nearest neighbors, $J_{x,y}$. In this work $J_{x,y} = \pm 1$ with 50% probability. Each assignment of the $\{J_{x,y}\}$ will be named a *sample*, and, once it is fixed, it will never be varied [1].

The interaction energy for the spins is

$$\mathcal{H} = - \sum_{\langle x,y \rangle} J_{x,y} \sigma_x \sigma_y, \quad (1)$$

($\langle \dots \rangle$ denotes lattice nearest neighbors). The choice $J^2 = 1$ fixes our energy units. We work in the so-called quenched approximation: any quantity (either a thermal mean value or a time dependent magnitude, see below) is supposed to be computed *first* for a given assignment of the couplings. Only afterwards the resulting value is averaged over the $J_{x,y}$, which we denote by $\overline{(\dots)}$.³

The spins evolve in time with Heat-Bath dynamics (see, e.g., [38]), which belongs to the universality class of physical evolution. The starting spin configuration is taken to be fully disordered, to mimic the experimental *direct quench* protocol.

Note that the Hamiltonian (1) has a global \mathbf{Z}_2 symmetry (if all spins are simultaneously reversed $\sigma_x \rightarrow -\sigma_x$ the energy is unchanged). This symmetry gets spontaneously broken in three dimensions upon lowering the temperature at the SG transition at $T_c = 1.109(10)$ [39].⁴

Finally, let us recall that the average over the coupling constants induces a non dynamical gauge symmetry [40]. Let us choose a random sign per site $\varepsilon_x = \pm 1$. Hence, the energy (1)

³ In principle, one should average many thermal histories for each sample and then compute the average over the disorder. In practice, errors can be largely reduced if one generates two histories per sample but generates more samples, since both sources of error are statistically independent. The claims on lack of self-averageness made in Sect. 2.2 depend critically on this choice. In fact, were one to simulate an infinite number of thermal trajectories per sample, the spin glass susceptibility would be self-averaging.

⁴ The alert reader will recall that the gauge symmetry of Eq. (2) forbids a spontaneous magnetization. Indeed, see Sect. 2.2, one needs to introduce an independently evolving copy of the spin configuration which promotes the symmetry to $\mathbf{Z}_2 \times \mathbf{Z}_2$. This is the symmetry which is actually spontaneously broken.

is invariant under the transformation

$$\begin{aligned} s_x &\longrightarrow \varepsilon_x s_x, \\ J_{x,y} &\longrightarrow \varepsilon_x \varepsilon_y J_{x,y} \end{aligned} \quad (2)$$

Since the gauge transformed couplings $\varepsilon_x \varepsilon_y J_{x,y}$ are just as probable as the original ones, the quenched mean value of an arbitrary function of the spins $O(\{s_x\})$ is identical to that of its gauge-average $\sum_{\{\varepsilon_x = \pm 1\}} O(\{\varepsilon_x s_x\}) / 2^{L^D}$, which typically is an uninteresting constant value. Constructing non trivial gauge-invariant observables is the subject of the next subsection.

2.2 Observables

A standard way of forming operators that are gauge-invariant under (2) is to consider real replicas. These are two statistically independent systems, $\{\sigma_x^{(1)}\}$ and $\{\sigma_x^{(2)}\}$, evolving in time with the very same set of couplings. Their (obviously gauge-invariant) overlap field at time t_w is

$$q_x(t_w) = \sigma_x^{(1)}(t_w) \sigma_x^{(2)}(t_w). \quad (3)$$

A slight modification consists in using just one of the real replicas, say $\{\sigma_x^{(1)}\}$, but considering times t_w and $t + t_w$

$$c_x(t, t_w) = \sigma_x^{(1)}(t + t_w) \sigma_x^{(1)}(t_w). \quad (4)$$

In many of the quantities defined below using $c_x(t, t_w)$, one may obviously gain statistics by averaging over the two real replicas. We have done so whenever it was possible, but this will not be explicitly indicated. We consider three types of quantities:

1. Single-time global quantities:

- Time-dependent energy density ($N = L^D$ is the number of spins in the lattice)

$$e(t_w) = -\frac{1}{N} \sum_{\langle x,y \rangle} J_{x,y} \sigma_x(t_w) \sigma_y(t_w). \quad (5)$$

Recall that $\langle x,y \rangle$ indicates summation restricted to lattice nearest neighbors.

- The spin glass susceptibility $\chi_{SG}(t_w)$ is defined in terms of the SG order parameter

$$q(t_w) = \frac{1}{N} \sum_x q_x(t_w). \quad (6)$$

Of course, the quenched mean value $\overline{q(t_w)}$ vanishes in the nonequilibrium regime where the system size is much larger than the coherence length $\xi(t_w)$. The susceptibility

$$\chi_{SG}(t_w) = N \overline{q^2(t_w)}, \quad (7)$$

steadily grows with the size of the coherent domains. Note that fluctuation-dissipation relations imply that χ_{SG} is basically the nonlinear magnetic susceptibility.

2. Two-times global correlation functions:

- Spin-spin correlations:

$$C(t, t_w) = \overline{\frac{1}{N} \sum_x c_x(t, t_w)}. \quad (8)$$

The function $C(t, t_w)$ carries many meanings:

- (a) If the first argument t_w is held fixed, and $C(t, t_w)$ is studied as t grows, it is just the thermoremanent magnetization. Indeed, because of the symmetry (2) the uniform configuration that would have been enforced by holding the spin glass in a strong external magnetic field can be gauged to the spin configuration found at time t_w after a random start.
- (b) On the other hand, in the pseudoequilibrium regime $t \ll t_w$, the (real part of the) magnetic susceptibility at frequency $\omega = 2\pi/T$ is given by the fluctuation-dissipation formula $(1 - C(t, t_w))/T$.
- (c) Another point we shall be concerned with is the computation of the SG order parameter. It may be defined from the translationally invariant time sector⁵

$$C_\infty(t) = \lim_{t_w \rightarrow \infty} C(t, t_w), \quad (9)$$

as

$$q_{\text{EA}} = \lim_{t \rightarrow \infty} C_\infty(t). \quad (10)$$

The computation of q_{EA} is notoriously difficult [26]. Note that other authors [27] subtract q_{EA} from $C_\infty(t)$ in such a way that it tends to zero for large t .

- The link correlation function

$$C_{\text{link}}(t, t_w) = \overline{\frac{1}{3N} \sum_{\langle x,y \rangle} c_x(t, t_w) c_y(t, t_w)}, \quad (11)$$

carries information on interfaces. Indeed, consider a coherent spin-flip in a domain half of the system size. This will induce a dramatic change in $C(t, t_w)$. On the other hand, the change in C_{link} will be concentrated at the lattice links that are cut by the surface of the flipped domain. If the geometry of this flipped region is that of a compact object with a vanishing surface to volume ratio, C_{link} will remain basically unchanged.

3. Space dependent correlation functions:

- Single time correlation function:

$$C_4(\mathbf{r}, t_w) = \overline{\frac{1}{N} \sum_x q_x(t_w) q_{x+\mathbf{r}}(t_w)}. \quad (12)$$

The long distance decay of $C_4(\mathbf{r}, t_w)$ defines the coherence length:

$$C_4(\mathbf{r}, t_w) \sim \frac{1}{r^a} f(r/\xi(t_w)). \quad (13)$$

⁵ By analogy, one may define a μ time sector by the limit $C_\infty^{(\mu)}(s) = \lim_{t_w \rightarrow \infty} C(st_w^\mu, t_w)$. The translationally invariant sector is just $\mu = 0$. In the range $0 < s < \infty$ the correlation function varies in $q_{\text{EA}} < C_\infty^{(\mu=0)}(s) < 1$. Full Aging [3] would imply that when $0 < s < \infty$, $C_\infty^{(\mu=1)}(s)$ goes from q_{EA} to 0. At the present moment, it is unclear whether the full range of variation of the correlation function, $0 < C < 1$, may be covered with just two time sectors.

The exponent a is relevant, because C_4 at distances $\xi(t_w)$ tends to zero as $\xi(t_w)^{-a}$. For coarsening systems, because $a = 0$, the order parameter does not vanish inside a domain. For the Ising SG in three dimensions the exponent was found to be $a \approx 0.4$ [33, 41] (see Sect. 3.2 for details). The long distance damping function f seems to decay faster than exponentially, $f(x) = \exp[-x^\beta]$ with $\beta \sim 1.5$ [10, 11]. Note as well that, at the critical point, a is related to the anomalous dimension, the latest estimate being $a(T_c) = 1 + \eta = 0.625(10)$ [39]. The physical origin for a nonzero a below T_c is in the replicon mode. In fact, it was conjectured that for all $T < T_c$, $a(T) = a(T_c)/2$ [22]. In [33] we found values not far from this prediction. Note that the exponent a is discontinuous at T_c [45].

- The two-time spatial correlation function (see [27, 28])

$$C_{2+2}(\mathbf{r}, t, t_w) = \overline{\frac{1}{N} \sum_{\mathbf{x}} [c_{\mathbf{x}}(t, t_w) c_{\mathbf{x}+\mathbf{r}}(t, t_w) - C^2(t, t_w)]}, \quad (14)$$

(one could also subtract $\overline{C(t, t_w)}^2$, but due to the self-averaging character of C this leads to the same thermodynamic limit). This correlation function is rather natural for the structural glasses problem, see for instance [42], where an adequate order parameter is unknown.

There is a simple probabilistic interpretation of C_{2+2} . Let us call a *defect* a site where $c_{\mathbf{x}}(t, t_w) = -1$ and let $n(t, t_w)$ be the density of these defects. We trivially have $C(t, t_w) = 1 - 2n(t, t_w)$. The conditional probability of having a defect at site $\mathbf{x} + \mathbf{r}$ knowing that there already is a defect at site \mathbf{x} is $n(t, t_w)g(\mathbf{r})$, where the defects' pair-correlation function is $g(\mathbf{r})$. Hence, $C_{2+2}(\mathbf{r}, t, t_w)$ is just $4n^2(t, t_w)(g(\mathbf{r}) - 1)$.

The long distance decay of $C_{2+2}(\mathbf{r}, t, t_w)$ defines the correlation length $\zeta(t, t_w)$ ⁶

$$C_{2+2}(\mathbf{r}, t, t_w) \sim \frac{1}{r^b} g(r/\zeta(t, t_w)). \quad (15)$$

Basically nothing is known on exponent b nor on the long distance damping function g . In [27, 28], this decay was fitted with $b = 0$ and $g(x) = e^{-x}$, but the smallness of the found correlation lengths $\zeta(t, t_w) < 2$ for $t + t_w \leq 1.3 \times 10^8$ [27, 28], does not permit strong claims. In the structural glasses context [42], one tries to interpret $\zeta(t, t_w)$ as a coherence length such as $\xi(t_w)$, rather than as correlation length. As we shall empirically show, this might be very reasonable in the limit $t \gg t_w$.

In an RSB framework, the relaxation within a single state corresponds to the range $q_{EA} < C(t, t_w) < 1$ (the further decay of $C(t, t_w)$ corresponds to the exploration of new states). This regime is quite naturally identified with the condition that $\zeta(t, t_w) \ll \xi(t_w)$. In fact, q_{EA} yields the (correlated) percolation threshold for defects.

Sometimes we will find it useful to change variables from t to C . This is always feasible, because $C(t, t_w)$ is a monotonically decreasing function of t for fixed t_w . The accuracy of our numerical data allows this change of variable without difficulty (we have used a cubic spline, since the function $C(t, t_w)$ was sampled at a selected set of times).

⁶ The difference between coherence and correlation length is a subtle one. In this work, we shall reserve the name ‘coherence length’, which is computed from a non-connected correlation function, Eq. (12), for the typical size of the coherent domains. The correlation length, which is computed from a connected correlation function, Eq. (14), refers to the characteristic length for defect correlation. In particular, the coherence length diverges when $t_w \rightarrow \infty$, while the correlation length may or may not diverge in that limit.

Finally, note that C_{2+2} is the difference of two statistically correlated quantities (hence, the statistical error in the difference may be expected to be smaller than that for each of the two terms). This can be adequately taken into account by means of a jackknife procedure (see, e.g., [38]).

All the quantities defined so far are self-averaging (i.e., their relative errors for a fixed number of samples decrease as $N^{-1/2}$), with the notorious exception of $\chi_{SG}(t_w)$. This fact provides justification for the standard strategy in nonequilibrium studies (both numerical and experimental!) of averaging results over very few samples.

Self-averageness stems from the fact that the computed/measured quantities are averages of local observables taken over the full system (which provides a number of statistically independent summands of the order of $L^D/\xi^D(t_w)$). The exception, $\chi_{SG}(t_w)$ (7), is actually non local as it is the integral over the whole system of $C_4(\mathbf{r}, t_w)$. Indeed, the central limit theorem suggests that the probability distribution function of $q(t_w)$ should tend to a Gaussian when $L \rightarrow \infty$. Hence, the variance for $\chi_{SG}(t_w)$ is $\sim 2\chi_{SG}^2(t_w)$ in the limit of a large system.

2.3 Simulation details

The *Janus* computer [32] can be programmed for the simulation of the single spin flip Heat Bath dynamics up to a very large number of lattice sweeps (units of Monte Carlo time) for systems of linear sizes up to $L \sim 100$.⁷

We have spent the most effort in simulating the dynamics of the model described by Eq. (1) in the direct quench protocol described in the Introduction, for several runs of about a hundred samples of linear size $L = 80$ and up to 10^{11} Monte Carlo steps (we recall that a single step corresponds to roughly 1 picosecond of time in the real world). Details of our simulations are given in Table 1. We extend here the analysis of the simulations reported on [33], but additional simulations have also been carried out. Most notably, we simulated 768 new samples of size $L = 80$ at $T = 0.7$ up to 10^{10} in Monte Carlo time, which have been useful to improve and test the statistical accuracy in some aspect of our analysis.

We wrote to disk the spin configurations at all times of the form $[2^{i/4}] + [2^{j/4}]$, with integer i and j (the square brackets stand for the integer part). Hence, our t and t_w are of the form $[2^{i/4}]$. Nevertheless, we computed C_{2+2} only for powers of two, due to the increased computational effort.

A final note on the time span of our runs. Much to our surprise, we found in [33] that, even for our very large systems, finite size effects in the coherence length can be resolved with our statistical accuracy. In this work, we have restricted ourselves to the time window that is not affected by them. The single exception will be in the analysis of energy relaxation, Sect. 5.2, where this range is too short. Nevertheless, we have explicitly checked that the energy suffers from smaller finite size effects than the coherence length.

2.4 Fits for extremely correlated data

Computing the best fit parameters and estimating errors from extremely correlated data sets presents a common, and still not satisfactorily solved, difficulty in many numerical studies. For instance, our study of $C(t, t_w)$ requires considering approximately 10^4 random variables

⁷ The overall parallel update rate for $L = 80$ systems of the whole Janus —256 nodes—is 78 femtoseconds per spin.

L	T	MC steps	N_s
80	0.6	10^{11}	96
80	0.7	10^{11}	63
80	0.8	10^{11}	96
80	0.9	2.8×10^{10}	32
80	1.1	4.2×10^9	32
80	1.15	2.8×10^{10}	32
80	0.7	10^{10}	768
40	0.8	2.2×10^8	2218

Table 1 Parameters of our simulations. The overall *wall-clock* time needed was less than six weeks. We highlight with boldface the simulations performed after completion of [33]. Recall that we take the critical temperature from [39], $T_c = 1.109(10)$. The full analysis of spin configurations was performed offline.

extracted from a set of only 63–768 samples. The standard approach, computing the covariance matrix and inverting it, fails because this matrix is necessarily singular.⁸ In this paper we shall follow an empirical procedure. We shall consider only the diagonal part of the covariance matrix in order to minimize χ^2 when performing fits. Unless otherwise indicated, we shall always use this diagonal χ^2 in the rest of the paper. Yet, in order to take correlations into account we shall perform this procedure for each jackknife block and later on compute error estimates from their fluctuations. As we have run simulations with both 63 (from [33]) and 768 samples for $T = 0.7$, we are in a position to test this method by comparing the results obtained and the ones to be expected for 63 samples (see Sect. 3.2).

The main drawback of this approach is that the standard χ^2 test of fit likelihood cannot be applied blindly. Of course, were the exact fitting function known, the average value of diagonal χ^2 should be 1 per degree of freedom. Yet, since the obtained fitting function may coherently fluctuate with the numerical data, we shall encounter anomalously low values of diagonal χ^2 . We examine this problem in Sect. 3.2, empirically finding that χ^2 behaves as if there were many fewer degrees of freedom than what one would expect.

3 Integral estimators of characteristic length scales

The need to estimate characteristic length scales, such as $\xi(t_w)$ or $\zeta(t, t_w)$ is a recurrent theme in lattice gauge theory and statistical mechanics. The more straightforward method is to consider a particular functional form for the long distance damping function in Eqs. (13) or (15). One of the problems with this approach, already identified in the study of equilibrium critical phenomena, is that it is extremely difficult to extract from numerical data *simultaneously* the length scale and the exponent for the algebraic decay. Note that quite often computing the exponent is as important as extracting the length scale to draw physical conclusions. The situation worsens if the functional form is only an educated guess, which is precisely our case. Furthermore, numerical data for the correlation function at different lattice sites suffer from dramatic statistical correlations, which complicates fitting procedures.

A different approach, the use of integral estimators, has been known since the 1980s [34]; but only in the mid 1990s (see e.g. [35, 36]) it was realized that it provided an enormous

⁸ Consider computing the covariance matrix for a set of N_O random variables from $N_s < N_O$ samples. If the $N_s \times N_O$ numbers are disposed on a rectangular matrix, it is clear that the last $N_O - N_s$ rows (reordering the rows if necessary) are a linear combination of the others. In other words, the results are indistinguishable from the ill-conditioned situation where these last $N_O - N_s$ random variables are the very same linear combination of the first ones. Once this is realized it is trivial to show that the range of the size $N_O \times N_O$ covariance matrix is at most N_s .

simplification. The use of integral estimators for the length scale enables determinations of exponents such as a in Eq. (13), which are completely independent from the functional form of the long distance damping. The only place left for systematic errors is in finite size effects or in scaling corrections (when the considered range for the variation of length scales such as $\xi(t_w)$ is too small). As for the determination of the length scale itself, integral estimators are guaranteed to produce numbers that scale as the inaccessible *true* $\xi(t_w)$, provided that it is large enough.

The fact that the correlation functions that will be considered here, C_4 and C_{2+2} , are self-averaging in a nonequilibrium context provides an impressive error reduction, which is not accessible for equilibrium studies.

Our chosen example to explain the method will be that of C_4 and the determination of the coherence length and of the exponent a .

3.1 The coherence length

Cooper *et al.* [34] suggested the second moment determination of the characteristic length,

$$\xi^{(2)}(t_w) \equiv \frac{1}{\sqrt{2} \sin \pi/L} \left[\frac{\hat{C}_4(0, t_w)}{\hat{C}_4(\mathbf{k}_{\min}, t_w)} - 1 \right]^{1/2}, \quad (16)$$

where $\hat{C}_4(\mathbf{k}, t_w)$ is the Fourier transform of $C_4(\mathbf{r}, t_w)$, and \mathbf{k}_{\min} is the minimal non-vanishing wave vector allowed by boundary conditions ($\mathbf{k}_{\min} = (2\pi/L, 0, 0)$ or permutations). Notice that $\chi_{\text{SG}}(t_w) = \hat{C}_4(0, t_w)$. As can be readily seen, in the thermodynamic limit this is equivalent to

$$\xi_{L=\infty}^{(2)}(t_w) = \sqrt{\frac{\int d^D \mathbf{r} r^2 C_4(\mathbf{r}, t_w)}{\int d^D \mathbf{r} C_4(\mathbf{r}, t_w)}}. \quad (17)$$

The denominator in this equation is just the SG susceptibility (7) which, as we said in Sect. 2.2, does not self-average (and neither does the numerator). Because of this, if one were to follow this method, a very large number of samples would be needed.

We would like to have a better statistically behaved definition of $\xi(t_w)$. In order to get it, we start by considering the integrals⁹

$$I_k(t_w) \equiv \int_0^{L/2} dr r^k C_4(r, t_w). \quad (18)$$

As we are going to work in the thermodynamical limit, we are interested in the regime $L \gg \xi(t_w)$, so we can safely reduce the upper integration limit from ∞ to $L/2$.

With this notation and assuming rotational invariance, the second moment coherence length is just

$$\xi_{L=\infty}^{(2)}(t_w) \simeq \sqrt{\frac{I_{D+1}(t_w)}{I_{D-1}(t_w)}}. \quad (19)$$

⁹ In what follows $C_4(r, t_w)$ stands for $C_4(\mathbf{r}, t_w)$, with $\mathbf{r} = (r, 0, 0)$ and permutations. As we shall see in Sect. 3.3, using an average over spherical shells does not achieve a significant reduction of statistical errors in our chosen estimator for the coherence length.

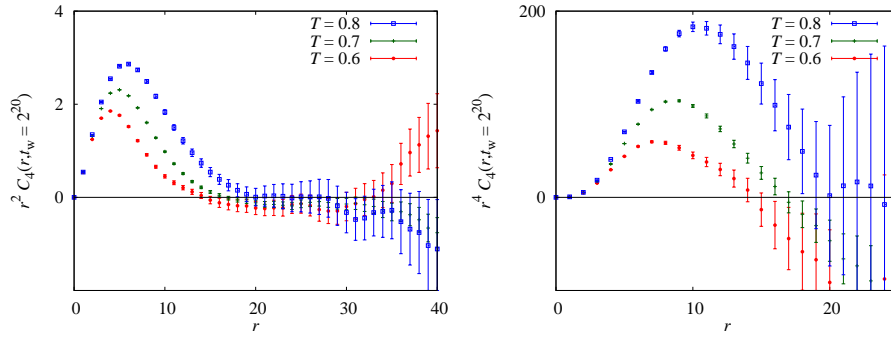


Fig. 1 The spatial autocorrelation of the overlap field for $t_w = 2^{20}$ and three subcritical temperatures, as computed in our $L = 80$ lattice. On the left panel we show $r^2 C_4(r, t_w)$, recall (18), while on the right one we show $r^4 C_4(r, t_w)$ (mind the different scales). While the signal to noise ratio of both quantities falls equally rapidly, the problem is less severe for the computation of $I_2(t_w)$ since the maximum there is not in the noise dominated region. The curve for $T = 0.7$ is the average of 768 samples, while those of $T = 0.6$ and $T = 0.8$ are computed from 96 samples.

We also recall that in [23] it was proposed to identify $\xi(t_w)$ with $I_0(t_w)$,¹⁰ but this would only be appropriate for $a = 0$. For a correlation function following the scaling law (13), one can use a more general definition, because $I_k(t_w) \propto [\xi(t_w)]^{k+1-a}$:

$$\xi_{k,k+1}(t_w) \equiv \frac{I_{k+1}(t_w)}{I_k(t_w)} \propto \xi(t_w). \quad (20)$$

Definitions such as (16) and (20) suffer from systematic errors because equation (13) is only an asymptotic formula for large values of r . Therefore, the systematic errors in these definitions can be reduced by considering a large value of k (since the r^k factor would suppress the deviations at short distances). However, there is also the issue of statistical errors to consider. As we can see in Fig. 1, a large power of r pushes the maximum of $r^k C_4(r, t_w)$ into the region where $r \gg \xi(t_w)$ and the signal to noise ratio of the correlation function is extremely low. Because of this, a compromise in the choice of k is needed. Our preferred option is $\xi_{1,2}(t_w)$.

Even though our use of $\xi_{1,2}(t_w)$ instead of $\xi^{(2)}(t_w)$ already mitigates the statistical problems in the integration of $C_4(r, t_w)$, we can still improve the computation. As can be plainly seen in Fig. 1, $r^2 C_4(r, t_w)$ starts having very large fluctuations only at its tails, where the contribution to the integral is minimal. To take advantage of this fact, we are going to use a self-consistent integration cutoff (a method applied before in the study of correlated time series [43]). We only integrate our data¹¹ for $C_4(r, t_w)$ up to the point where this function first becomes less than three times its own statistical error. Of course, while this method provides a great reduction in statistical errors, it does introduce a systematic one. To avoid it, we estimate the small contribution of the tail with a fit to

$$C_4(r, t_w) = \frac{A}{r^{0.4}} \exp \left[-\left(r/\xi^{\text{fit}}(t_w) \right)^{1.5} \right]. \quad (21)$$

¹⁰ The authors of [23] carefully discussed the interplay of the integration limits in (18) and the boundary conditions. Since we restrict ourselves to $L \gg \xi(t_w)$, this is immaterial to us.

¹¹ As our (somewhat arbitrary, yet irrelevant) choice of quadrature method we have chosen to interpolate the data with a cubic spline, whose integral can be exactly computed.

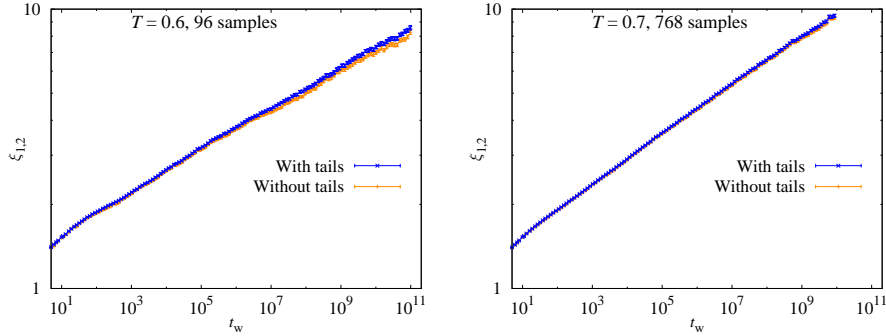


Fig. 2 Left: Result of computing $\xi_{1,2}$ in two different ways for our 96 samples at $T = 0.6$. In the orange curve (color online) we stop the integration at the cutoff point where relative error of C_4 is greater than one third. In the blue curve (color online) we estimate the contribution of the tail from that point on extrapolating with a fit to (21). The difference is small, but with the second method the power law behavior of $\xi_{1,2}(t_w)$ lasts longer. **Right:** Same plot for our 768 samples at $T = 0.7$. With the increased statistics this extrapolation is not as important and both curves are compatible for the whole simulation. With the 63 samples of [33], the tail contribution is as significant as in the left panel.

Notice that this is just the scaling function (13), using $f(x) = \exp[-x^{1.5}]$ as our damping function and $a = 0.4$. Of course, while this fit is used to estimate the contribution of the interval $[r_{\text{cutoff}}, L/2]$, we actually perform the fitting for $3 \leq r \leq \min\{15, r_{\text{cutoff}}\}$, where the signal is still good. This last step is important for large t_w (see Fig. 2).

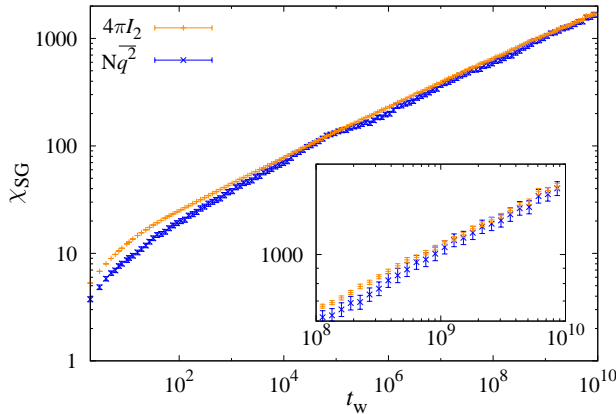


Fig. 3 The SG susceptibility $\chi_{\text{SG}}(t_w)$ for our 768 samples at $T = 0.7$ computed from q^2 and from the integral I_2 : $\chi_{\text{SG}}(t_w) = \bar{Nq^2(t_w)} = 4\pi I_2(t_w)$. The main difference between the two determinations is that the second one has been computed with a self-consistent cutoff. As we can see, even though both curves are compatible, the integral one is much more precise. The inset details the upper right corner.

As a consistency check of this method and as a demonstration of its enhanced precision we can consider the SG susceptibility (7). This observable, $\chi_{\text{SG}}(t_w) = \bar{Nq^2(t_w)}$, coincides with $4\pi I_2(t_w)$ in the presence of rotational invariance. We have plotted both expressions as a function of time in Fig. 3. The only systematic discrepancy between the two is at short times,

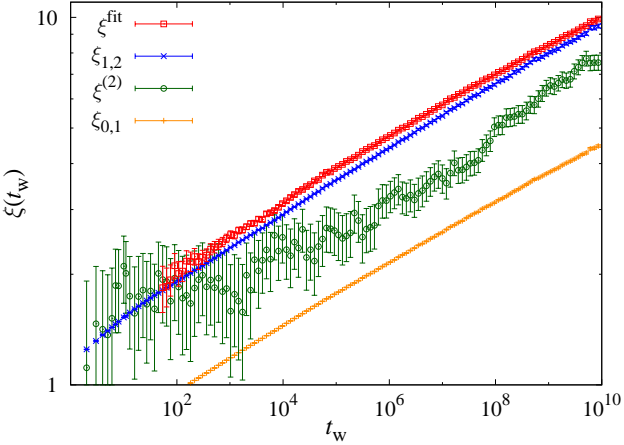


Fig. 4 Comparison of our integral estimators $\xi_{0,1}$ and $\xi_{1,2}$, Eq. (20), with the second moment estimate $\xi^{(2)}$ and the result ξ^{fit} of a fit to (21), with $a = 0.4$. All the curves become parallel at large t_w , but the integral estimators have much smaller errors. All curves are for our 768 samples at $T = 0.7$.

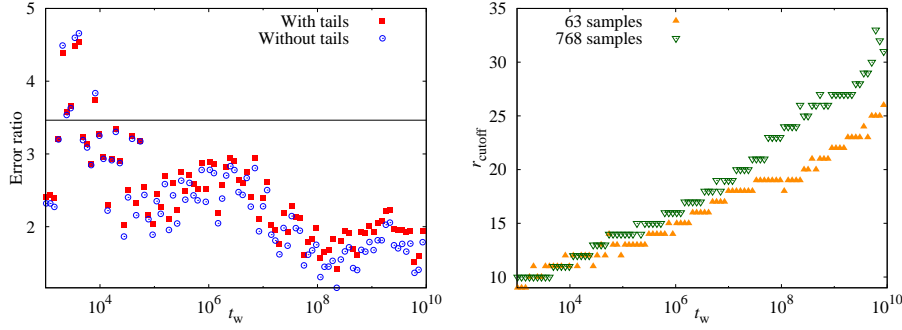


Fig. 5 **Left:** Ratio of the errors in $\xi_{1,2}(t_w)$ for the simulations at $T = 0.7$ with the 63 samples of [33] and those of our simulations with 768 new samples (see text for discussion). The extrapolation to include the tails in the integrals is immaterial for this ratio. The horizontal line is $\sqrt{768/63} \approx 3.46$. **Right:** Cutoff of the I_k integrals as a function of time for both simulations.

when the system cannot be considered rotationally invariant (see Sect. 3.3). However, the integral determination $4\pi I_2(t_w)$ is much more precise for the whole span of our simulation.

As a second check, we have plotted in Fig. 4 the integral estimators $\xi_{0,1}(t_w)$ and $\xi_{1,2}(t_w)$, together with the traditional second moment estimate $\xi^{(2)}$ and the result of a fit to (21). As we can see, all determinations are indeed proportional, but the integral estimators are much more precise.

Finally, we address the issue of our error estimates by comparing our data at $T = 0.7$ for the 63 samples of [33] with our new simulations with 768 samples. We have explicitly checked that the errors in $C_4(r, t_w)$, computed with the jackknife method, scale as the inverse of the square root of the number of samples, within errors (for Gaussian distributed data, the relative statistical error in the error estimate is $\sim 1/\sqrt{2N_{\text{samples}}}$). The fact that C_4 verifies this basic expectation is a demonstration that large deviations, which would be missed for a small number of samples, do not appear, even for t_w as large as 10^{10} . On the other hand,

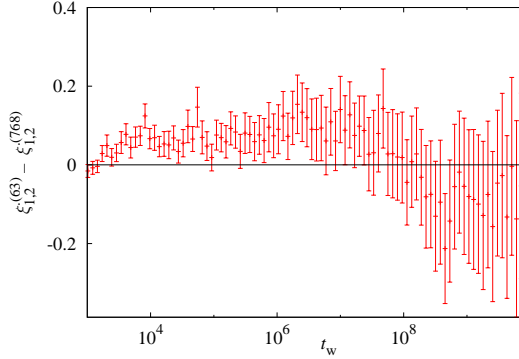


Fig. 6 Difference between the coherence length $\xi_{1,2}(t_w)$ computed with the 63 samples of [33] and with the 768 new samples (the errors are the quadratic sum of those for each simulation). Both curves are compatible in the whole time range. Mind the dramatic statistical correlation in the sign of this difference.

the behavior of statistical errors in integrals with a dynamically fixed cutoff is not that simple [43]. In our case, the ratio of the errors in $\xi_{1,2}(t_w)$ (Fig. 5, left) is around 30% below the Gaussian expectation. We have checked that a similar effect arises in the computation of $I_2(t_w)$ and that the effect of the tails is immaterial. In fact, this deviation is entirely due to the difference in the dynamical cutoffs of both simulations, Fig. 5, right. Whenever the cutoff coincides, the error ratio is in the expected region around $\sqrt{768/63} \approx 3.46$. The overall consistency of our error determinations is demonstrated by Fig. 6.

3.2 The algebraic prefactor

One of our main goals is to provide a precise estimate of the exponent a for the algebraic part of C_4 , see equation (13). Equilibrium methods [36] are not well suited to a nonequilibrium study in the thermodynamic limit. Instead, we introduce here the method used, but not explained, in [33].

The starting point is the realization that $I_1 \propto \xi_{1,2}^{2-a}$, which would indicate that a can be obtained from a power law fit of I_1 as a function of the coherence length. Furthermore, the large statistical correlation between I_1 and $\xi_{1,2}$ can be used to reduce the statistical errors in a . However, such a fit would be quite problematic, as we would have errors on both coordinates (the correlation of the data already poses a nontrivial problem with errors in just one coordinate, see Sect. 2.4). Instead, we fit separately $I_1(t_w)$ and $\xi_{1,2}(t_w)$ to power laws in the waiting time. This way, if

$$I_1(t_w) = At_w^c, \quad \xi(t_w) = Bt_w^{1/z}, \quad (22)$$

we have $a = 2 - cz$. This relation holds for each jackknife block, which lets us take full advantage of the correlations.

Following this method, we obtain the results in Table 2. In [33] (first four rows of Table 2) we quoted the results for a fitting range of $\xi_{1,2} \in [3, 10]$, which is perfectly adequate for $T = 0.6, 0.8$ and 1.1 . As we can see, χ^2 appears to be a bit too large for $T = 0.7$, but if we narrow the fitting range it becomes reasonable and a does not change.

T	N_{samples}	$[\xi_{\min}, \xi_{\max}]$	z	a	$\chi^2_{\xi}/\text{d.o.f.}$	$\chi^2_{I_1}/\text{d.o.f.}$
0.6	96	[3, 10]	14.06(25)	0.359(13)	41.7/82	49.0/82
		[3, 10]	11.84(22)	0.355(15)	82.7/81	131/81
0.7	63	[3.5, 10]	12.03(27)	0.355(17)	52.7/71	75.5/81
		[3, 10]	9.42(15)	0.442(11)	17.1/63	12.2/63
1.1	32	[3, 10]	6.86(16)	0.585(12)	18.7/46	26.1/46
		[3, 10]	11.45(10)	0.395(8)	86.9/76	269/76
0.7	768	[3.5, 10]	11.56(13)	0.397(10)	46.6/66	101/66
		[4, 10]	11.64(15)	0.397(12)	40.1/58	60.4/58
		[4.5, 10]	11.75(20)	0.394(14)	29.6/50	35.8/50

Table 2 Value of the dynamic exponent z and the algebraic prefactor a for several temperatures. The fitting range $\xi_{1,2} \in [3, 10]$, which worked for the smaller number of samples we had in [33], does not give good fits for I_1 with our enlarged statistics at $T = 0.7$ (the fits for the coherence length itself are still good). Nevertheless, if we increase ξ_{\min} to get reasonable values of $\chi^2_{I_1}/\text{d.o.f.}$ we see that the estimate of a does not change.

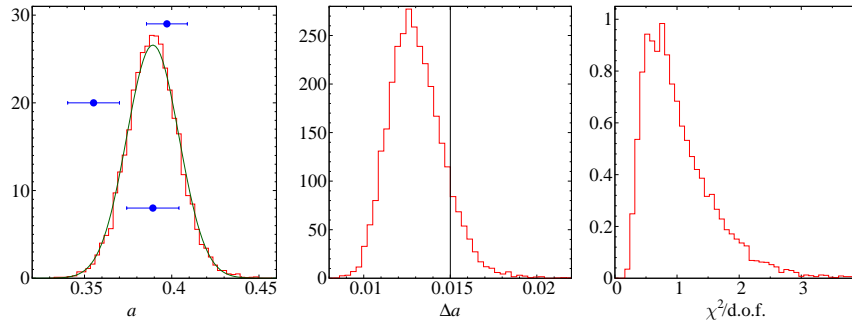


Fig. 7 Left: Probability density function $\rho(a)$ of the estimate of exponent a , Eq. (13), as obtained from a set of 63 samples. The dots with *horizontal* error bars are, from top to bottom: our best estimate with 768 samples, the value with the 63 samples of [33], and the mean and standard deviation of $\rho(a)$. The continuous line is a Gaussian distribution with the same mean and variance as $\rho(a)$. **Center:** As in left panel, for the jackknife errors Δa . The vertical line marks the standard deviation of $\rho(a)$. **Right:** Histogram of the $\chi^2/\text{d.o.f.}$ parameter for the χ^2 fit. In all three panels the fitting range to obtain a was taken as $\xi \in [3, 10]$.

As this is a very important magnitude, in this work we have increased the number of samples at $T = 0.7$ by a factor of 12 with respect to [33], (from 63 to 768 samples, with extra simulations that stop at $t_w = 10^{10}$, rather than 10^{11}). This not only allows us to provide a better estimate of a but we are now also able to check the soundness of the statistical procedure.

The first difficulty is that, with the corresponding reduction in statistical errors, the original fitting window no longer provides reasonable values of our diagonal χ^2 estimator. Instead, we have pushed the lower limit to $\xi \geq 4$ (see Table 2 for details). The new value of $a(T = 0.7)$ is

$$a(T = 0.7) = 0.397(12). \quad (23)$$

In accordance to the analysis of Fig. 5, the error has not decreased the factor $\sqrt{768/63}$ with the increase in statistics. One could say that the dynamic cutoff procedure has traded statistical uncertainty for a reduction in systematic errors. Another contributing factor to the large statistical error is the raising of the minimal coherence length included in the fit.

To understand whether the discrepancy between the new estimate of a and the one in [33] is due to a systematic effect or to a large fluctuation, we can use a Monte Carlo method. The probability distribution function of the estimates of a , as computed with 63 samples, can be obtained easily from our set of 768 samples. One randomly picks sets of 63 different samples and determines a and its jackknife error Δa for each of these sets (mind that there are $\binom{768}{63} \approx 2.2 \times 10^{93}$ possible combinations). We have done this 10 000 times and computed normalized histograms of both quantities (Fig. 7). Clearly enough, the estimate in [33] was a fluctuation of size 2.2 standard deviations, large but not unbelievably so. On the other hand we see that the jackknife method tends to slightly underestimate Δa for 63 samples (Fig. 7, center). Note as well that there seems to be a small bias (smaller than the error) on the estimate of a with only 63 samples (Fig. 7, left, compare the histogram with the uppermost horizontal point). There are two possible reasons for this. One is that a is obtained from raw data through a nonlinear operation. The other is that the larger the number of samples, the smaller the cutoff effects in the computation of $I_k(t_w)$.

It is amusing to compute as well the probability density of $\chi^2/\text{d.o.f.}$ for fits with 63 samples. We show in Fig. 7, right, that χ^2_ξ for the fit of the coherence length can be much larger than what one would naively expect for a fit with ~ 80 degrees of freedom.

3.3 Isotropy of $C_4(\mathbf{r}, t_w)$

In the previous section we neglected the issue of the isotropy of $C_4(\mathbf{r}, t_w)$. At all times we worked with radial functions $C_4(r, t_w)$, obtained by averaging the correlation at distance r along the three axes. In doing this, we ignored most of the N points that $C_4(\mathbf{r}, t_w)$ has for a given t_w . The main motivation for doing this is avoiding the computation of the whole correlation function, a task which in a naive implementation is $\mathcal{O}(N^2)$. Of course, due to the Wiener-Khinchin theorem, we can reduce this computation to the evaluation of two Fourier

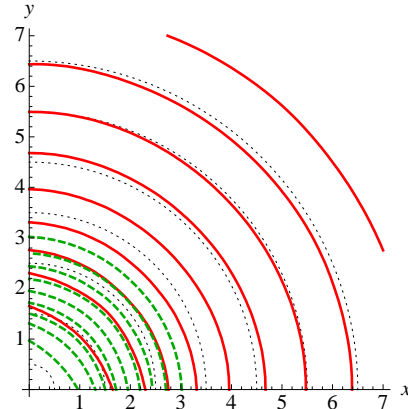


Fig. 8 Level curves $C_4(\mathbf{r}, t_w) = c$ for $c = 0.3$ (dashed lines) and $c = 0.1$ (solid lines) at $T = 0.6$ (dotted lines are circles, for visual reference). We have restricted ourselves to the $z = 0$ plane, for clarity. The innermost curve corresponds in both cases to $t_w = 4$ and the succeeding ones correspond to geometrically growing times ($t_w = 4 \times 16^j$). As we can see, the deviations from isotropy are mainly due to lattice discretization (i.e., functions of r), even though there is also a small dependence on time for curves of similar radii. The errors are smaller than the thickness of the lines (the interpolation to draw these continuous curves from our lattice data was performed with *Mathematica TM*).

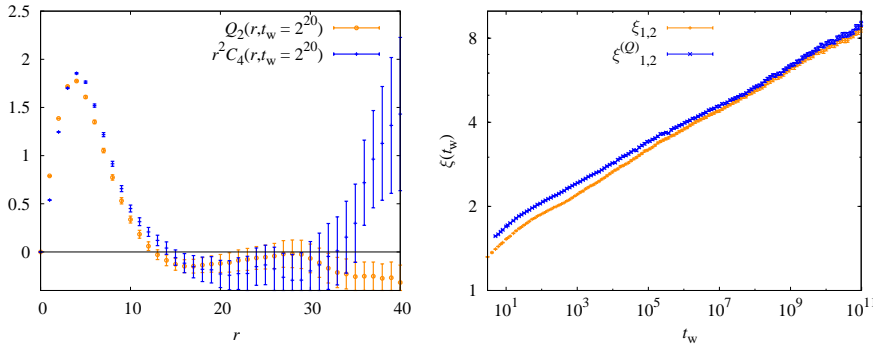


Fig. 9 **Left:** Comparison of $Q_2(r, t_w = 2^{20})$ with $r^2 C_4(r, t_w = 2^{20})$ for $T = 0.6$. The first quantity is obtained by averaging over spherical shells, while the second one considers only correlations along the axes. The behavior of Q_2 is better at the tails, but does not imply any gain in practice, as both functions are equally well behaved up to the cutoff point. **Right:** The coherence length computed with the whole correlation functions, $\xi_{1,2}^{(Q)}$, and with correlations along the axes, $\xi_{1,2}$. Both estimates coincide for large times.

transforms which, using an implementation of the FFT algorithm [44], is an $\mathcal{O}(N \log N)$ task.

We shall examine in this section whether the complete correlation functions are isotropic and whether we can take advantage of them to reduce the errors in our determination of the coherence length. The first question is answered by Fig. 8, where we compute the level curves $C_4(\mathbf{r}, t_w) = c$ for several values of c and t_w . As we can see, isotropy is recovered at quite small distances (remember we are only concerned with $\xi \gtrsim 3$).

In order to use our integral method for a three-dimensional $C_4(\mathbf{r}, t_w)$ we must first average it over spherical shells. We do this by defining the functions $Q_k(n, t_w)$,

$$Q_k(n, t_w) \equiv \frac{\sum_{|\mathbf{r}| \in [n, n+1]} |\mathbf{r}|^k C_4(\mathbf{r}, t_w)}{\sum_{|\mathbf{r}| \in [n, n+1]} 1}. \quad (24)$$

Notice that $Q_0(0, t_w) = C_4(0, t_w) = 1$ and that the division by the number of points is needed to average over the spherical shell. Now we can use $Q_k(r, t_w)$ in the same way we used $r^k C_4(r, t_w)$ in the previous section. The resulting coherence length $\xi_{1,2}^{(Q)}(t_w)$ would be expected to coincide with $\xi_{1,2}(t_w)$ in the large t_w limit, but have much smaller errors due to the large increase in statistics. As we can see from Fig. 9, however, the correlation among the points is so great that the gain in precision is insignificant.

We can conclude from this section that the usual approximation of considering $C_4(\mathbf{r}, t_w)$ isotropic is a well founded one and that it is safe, and statistically almost costless, to restrict ourselves to correlations along the axes, as we did in [33] and in the previous section. Nevertheless, the computation of the whole $C_4(\mathbf{r}, t_w)$ could be rewarding if one were to study I_k , with $k > 2$.

4 Characteristic length scales for dynamical heterogeneities

The concept of heterogeneous dynamics has been recently borrowed from structural glasses to describe non-local aging in Spin Glasses [27, 28]. A *coarse-grained* spin correlation func-

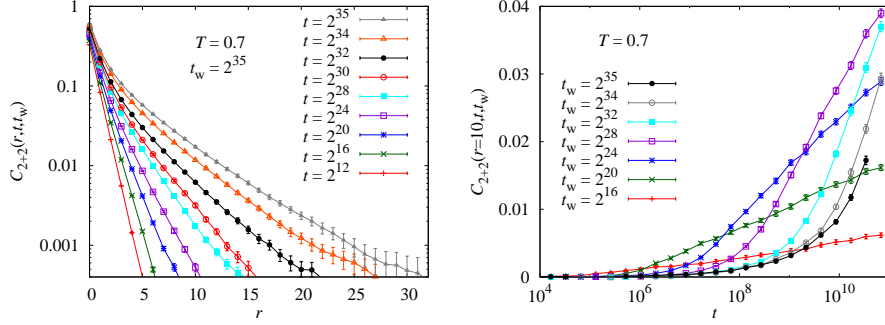


Fig. 10 **Left:** The two-time spatial correlation function $C_{2+2}(r, t, t_w)$ (see Eq. (14)) as a function of r , for a high value of $t_w = 2^{35}$, and several values of t . **Right:** $C_{2+2}(r, t, t_w)$ as a function of t and several values of t_w , fixing $r = 10$. Both figures are for our 63 sample simulation at $T = 0.7$.

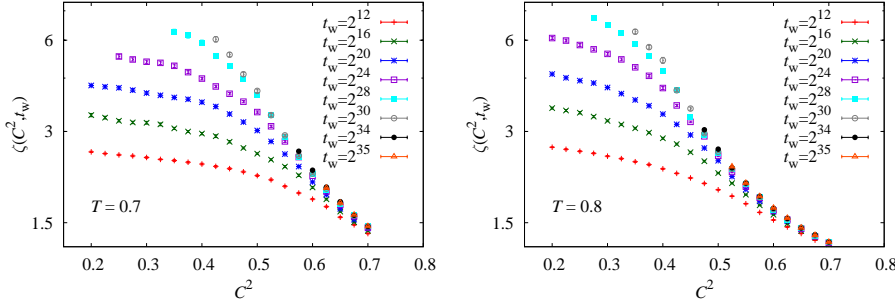


Fig. 11 **Left:** Coherence length $\zeta(C^2, t_w)$ as a function of C^2 for several values of t_w at $T = 0.7$ (63 samples). **Right:** As figure left, for $T = 0.8$ (96 samples).

tion may be defined for which the microscopic average is not performed on the overall volume but on cells of size ℓ^D . Non-uniform aging of the system results in spatial fluctuations of the coarse-grained correlation functions, that can be used to define a two-time dependent correlation length. In fact, at fixed system size and temperature one may study the *two-time* dependent distribution of the coarse-grained correlation function values or, equivalently, the distribution as a function of t_w and of the global spin-spin correlation function $C(t, t_w)$, Eq. (8): if the coarse-graining size ℓ^D is larger than the correlation length, then one should observe Gaussian statistics, while strong deviations from a Gaussian distribution are present in case of small ℓ^D [28]. Such dependence of the statistics on the coarse-graining size defines a crossover length $\zeta(C^2, t_w)$ interpreted as an aging (*two-time*) correlation length.

It has been observed [28] that such an aging correlation length may be obtained from the spatial decay of the *two-time two-site* correlation function C_{2+2} , Eq. (14); still, the authors of reference [28] could not measure ζ values greater than two lattice spacings. In this section we present data from our simulations on Janus showing correlation lengths for dynamical heterogeneities up to order ten lattice units. We show $C_{2+2}(r, t, t_w)$ for $t_w = 2^{35}$ and some values of t at temperature $T = 0.7$ in the left picture of Fig. 10 (as for C_4 , we denote by $C_{2+2}(r, t, t_w)$ the correlations along the axes). As one can see in this figure, at large times, correlations grow up to several lattice spacings.

In what follows it is convenient to eliminate the time t dependence in favor of the global spin-spin correlation function $C(t, t_w)$. For given t_w and C values, we obtain easily $t(t_w, C)$ because the monotonic time dependence of the (discrete measures of the) correlation function can be smoothly interpolated by means of cubic splines. Then, for each value of r , we must interpolate $C_{2+2}(r, t(C, t_w), t_w)$. As one can see in the right picture of Fig. 10 there is a sharp change in the t -derivative of C_{2+2} , so we had to resort to a linear interpolation in order to avoid the strong oscillations that a spline had suffered from. Once $C_{2+2}(r, t(C, t_w), t_w)$ has been interpolated at all r values, the methods of Sect. 3 allow us to estimate the correlation length $\zeta(C^2, t_w)$.

In the large correlation sector, i.e. $q_{\text{EA}}^2 < C^2$, and for large t_w , the correlation length $\zeta(C^2, t_w)$ approaches a t_w independent value. On the other hand, one expects that for small values of C^2 (that is, $C^2 < q_{\text{EA}}$) and large t_w , $\zeta(C^2, t_w)$ diverges as the coherence length $\xi(t_w)$ defined in Eq. (13) [29]. Such behavior is represented in Fig. 11, in which we plot ζ as a function of C^2 , at temperatures $T = 0.7$ and $T = 0.8$, for some values of t_w . It is also interesting to consider the ratio $R(C^2, t_w) = \zeta(C^2, t_w)/\xi(t_w)$ and study how its behavior as a function of C^2 changes with t_w . As pointed out above, for small values of C^2 and large t_w , we expect $R(C^2, t_w) \sim \text{const} > 0$. Moreover, since the coherence length $\xi(t_w)$ diverges for large t_w , $R(C^2, t_w)$ should vanish at large waiting times when $C^2 > q_{\text{EA}}^2$. In Fig. 12 we show $R(C^2, t_w)$ at temperatures $T = 0.6, 0.7$ and 0.8 . An interesting feature is the crossover between the two sectors $C^2 < q_{\text{EA}}^2$ and $C^2 > q_{\text{EA}}^2$. At $T = 0.8$ the q_{EA} is too small (see Table 4 in Sect. 5.1 below) to let us observe the small C^2 behavior described above. On the other side, data for $R(C^2, t_w)$ at $T = 0.6$ quickly approaches a constant value for small correlations. It seems that the larger t_w , the fastest the convergence to a constant, determining in this way a crossing point. However, these data suffer from large fluctuations that do not allow us to make any strong speculation on the crossings among curves at large values of t_w . Indeed, we know that $R(C^2, t_w)$ should vanish for large C^2 roughly as $1/\xi(t_w)$, but up to our knowledge, there is no reason for R , as a function of C^2 , to converge faster to a constant when t_w increases. In the bottom pictures of Fig. 12 we report the same data at $T = 0.7$, averaged on both 63 (left) and 768 samples (right). Even if simulations on larger sample statistics are not as long as those of the first 63 samples, the smoothing in the curves does not improve the crossing definition. In addition, we have not been able to find any clear scaling behavior of the crossing points with the waiting time.

Since at large times and small correlations $\zeta(C^2, t_w)$ and $\xi(t_w)$ only differ in a constant factor (which is also close to 1), one may expect that the behavior of the two-time, two-site correlators (Eq. (14)) should be analogous to that of the four point correlation function (Eq. (12)). We can then probe the long distance scaling of C_{2+2} with the same analysis performed in reference [33] (and in Sect. 3.2) for $C_4(r, t_w)$, Eq. (13). In particular, we can extract the exponent b of the algebraic prefactor in Eq. (15) and the dynamic exponent z_ζ , assuming a power-law growth for the correlation length:

$$\zeta(C^2, t_w) = A t_w^{1/z_\zeta}. \quad (25)$$

We fix C^2 to a T -dependent value, which is a value small enough to be below the q_{EA}^2 at all considered temperatures $T = 0.6, 0.7$ and 0.8 (C^2 values should be compared with q_{EA}^2 estimates given in Sect. 5.1), and large enough to have the necessary number of t_w points in order to obtain fair fits. We also had to impose a $\zeta_{1,2} \geq 3$ constraint to avoid the effects of lattice discretization. We did not impose any upper limit to ζ , whose values hardly reach 8 lattice spacings at $T = 0.8$ (even less at colder temperatures), and we expect that in the time sector considered the constraint imposed on ζ in reference [33] and in Sect. 3.2 would work as well as in that case.

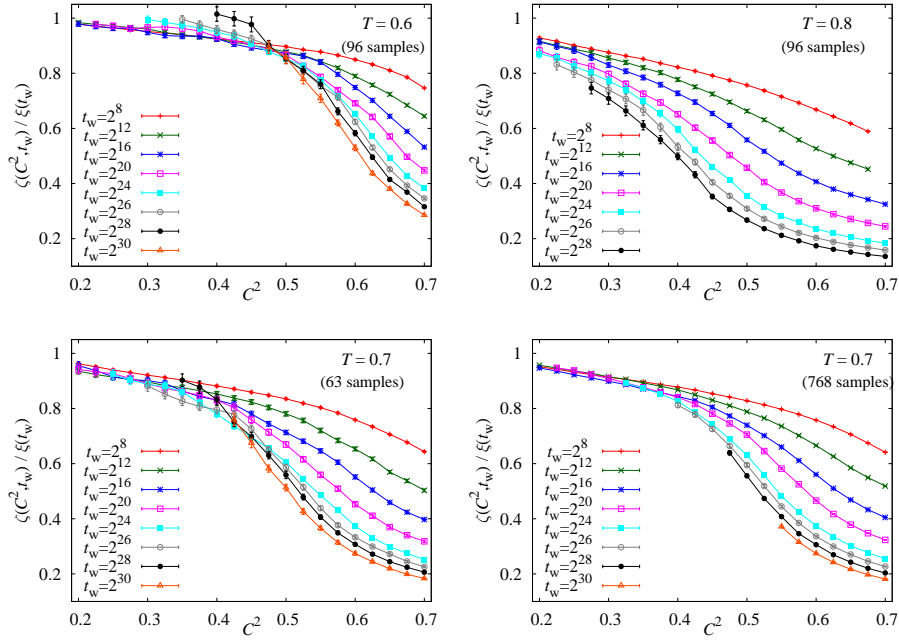


Fig. 12 Behavior of the ratio $R(C^2, t_w) = \zeta(C^2, t_w) / \xi(t_w)$ as a function of C^2 for several values of t_w . **Top left:** at our lowest temperature $T = 0.6$. **Top right:** at temperature $T = 0.8$. **Bottom left:** at temperature $T = 0.7$ averaged over 63 samples. **Bottom right:** same plot as bottom left, averaging over 768 samples.

T	C^2	z_ζ	b	$\chi_\zeta^2/\text{d.o.f.}$	$\chi_{t_1}^2/\text{d.o.f.}$
0.6	0.200	13.4(6)	0.43(4)	0.01/2	0.13/2
	0.325	12.8(4)	0.55(3)	7.16/7	4.45/7
0.7	0.200	11.14(20)	0.508(17)	0.69/3	0.37/3
	0.325	11.35(12)	0.642(9)	8.08/7	7.70/7
0.8	0.100	9.56(17)	0.497(13)	3.73/5	3.37/5
	0.175	10.12(13)	0.540(10)	7.15/8	7.91/8

Table 3 Value of the dynamic exponent z_ζ and exponent b for the algebraic prefactor, for three subcritical temperatures. We limited the fitting window constraining the fits to $\zeta_{1,2} \geq 3$. Data at $T = 0.7$ averaged over 768 samples.

We summarize the obtained values of b in Table 3, reporting results for the smallest C^2 attainable (that is, permitting reasonable fits) at all temperatures, as well as for larger values of C^2 , for which the number of t_w points allows for quite good fits. We see that b and z_ζ are slightly different from the values of a and z for the four point correlators presented in Sect. 3.2. Unfortunately our data do not permit a more precise determination for these exponents in the deep $C^2 < q_{EA}^2$ sector. In this respect, the determination of q_{EA} is a crucial issue (see Sect. 5.1).

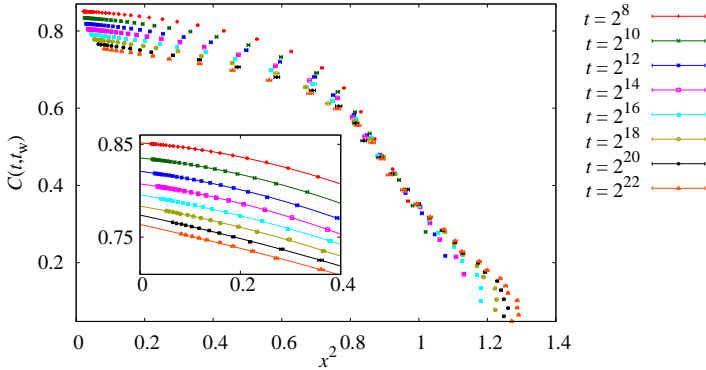


Fig. 13 The spin-spin correlation $C(t, t_w)$ as a function of $x^2 = (\zeta(t, t_w)/\xi(t_w))^2$ for $T = 0.7$. **Inset:** Close up of the small x^2 region and comparison with our quadratic fits.

5 The time correlation functions

5.1 The stationary part of $C(t, t_w)$

The naive computation of the stationary part of $C(t, t_w)$, $C_\infty(t)$ Eq. (9), suffers from an essential problem: how to know when t_w is large enough. The consideration of characteristic length scales may simplify this problem, as the limit $t_w \rightarrow \infty$ is equivalent to $\xi(t_w)^{-1} \rightarrow 0$.¹² However, the approach to this limit will be acutely t -dependent. Hence, it is better to consider a dimensionless variable,

$$x(t, t_w) = \frac{\zeta(t, t_w)}{\xi(t_w)}. \quad (26)$$

As we saw in Sect. 4, the correlation length $\zeta(t, t_w)$ quickly reaches a t_w -independent limit, so $x(t, t_w)$ is essentially $\xi^{-1}(t_w)$ in its natural units for each t . In fact, see Fig. 13 for our data at $T = 0.7$, the plot of $C(t, t_w)$ against $x^2(t, t_w)$ is pretty smooth for $x^2 \rightarrow 0$. Furthermore, the curves for different t become parallel as t grows, which suggests the existence of a smooth scaling function, $C(t, t_w) = C_\infty(t) + f(x^2)$. We have fitted the curves $C(t, x^2)$ for each t in the range $x^2 \leq 0.5$ to a quadratic polynomial (see inset to Fig. 13),

$$C(t, x^2) = C_\infty(t) + a_1(t)x^2 + a_2(t)x^4. \quad (27)$$

Unlike our treatment of the exponent a (Sect. 3.2), here we cannot skirt the issue of errors in both coordinates. As the effect of both errors is similar, we have performed a least squares fit and an a posteriori χ^2 test, Fig. 14, right. This χ^2 test was diagonal in the sense that we did not consider correlations among different pairs of times, but we did consider the covariance matrix for (x^2, C) at the same (t, t_w) . Our statement that the scaling curves in Fig. 13 become parallel is made quantitative in Fig. 14, left, which plots the coefficient $a_1(t)$ in equation (27).

The method described above has allowed us to compute $C_\infty(t)$ with remarkable accuracy for $t \lesssim 10^8$, see Fig. 15. We can now try to perform a second extrapolation, Eq. (10), and

¹² In what follows we shall always use the $\xi_{1,2}$ estimator.

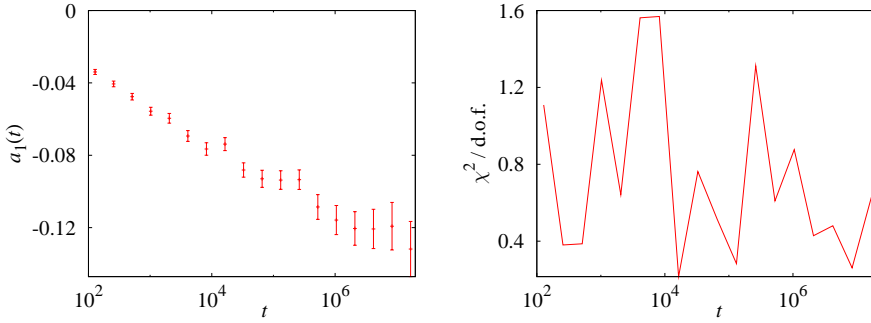


Fig. 14 **Left:** Slope at $x^2 = 0$ of the fitting curves (27) at $T = 0.7$ as a function of time. **Right:** Check of the fit quality using a χ^2 estimator that takes into account correlations only at equal (t, t_w) , but disregards correlations among different pairs of times.

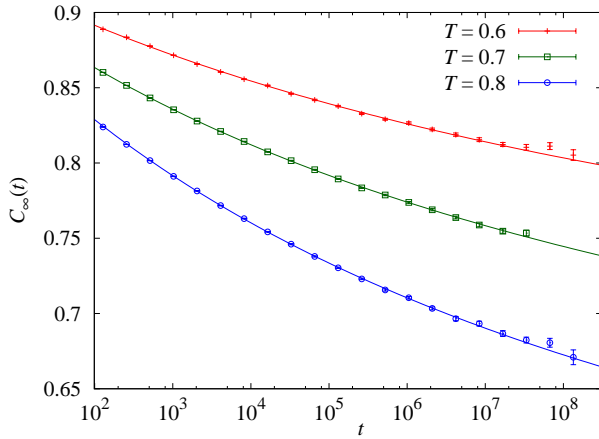


Fig. 15 Stationary component of $C(t, t_w)$, $C_\infty(t)$, obtained with the extrapolations in Figs. 13 and 14, for all our subcritical temperatures.

obtain the value of q_{EA} for each of our simulated temperatures. In order to do this we first tried a power law extrapolation

$$C_\infty(t) = q_{\text{EA}} + At^B. \quad (28)$$

This functional form yielded very good fits for $T = 0.6, 0.8$ but the values of the exponent B were very small, of about $B \sim -0.05$. Unfortunately, the smallness of B makes the extrapolation extremely risky. Just to be on the safe side and check explicitly that $q_{\text{EA}} > 0$, we have tried a logarithmic fitting function,

$$C_\infty(t) = q_{\text{EA}} + \frac{A}{B + \log t}. \quad (29)$$

This Ansatz lacks any theoretical basis, but since it is slower than any power law, we expect it to provide a lower bound on q_{EA} . On the numerical side, the logarithmic fit was as good as the power law (as determined by a χ^2 test). Nevertheless, as expected, it produced values of q_{EA} which were incompatible with those of equation (28) (see Table 4). Furthermore,

T	Fitting range	Logarithm		Power law	
		q_{EA}	$\chi^2/\text{d.o.f}$	q_{EA}	$\chi^2/\text{d.o.f}$
0.6	$[10^2, 10^8]$	0.607(16)	34.1/17	0.730(8)	5.7(4)
	$[10^3, 10^8]$	0.62(3)	7.23/14	0.733(14)	5.8(7)
	$[10^4, 10^8]$	0.62(5)	6.25/10	0.726(24)	5.4(12)
0.7	$[10^2, 10^8]$	0.497(10)	23.7/17	0.656(5)	6.16(18)
	$[10^3, 10^8]$	0.474(21)	18.9/14	0.637(11)	5.5(3)
	$[10^4, 10^8]$	0.49(5)	15.0/10	0.63(3)	5.4(9)
0.8	$[10^2, 10^8]$	0.371(13)	6.50/17	0.568(7)	6.56(20)
	$[10^3, 10^8]$	0.368(24)	5.53/14	0.556(12)	6.2(4)
	$[10^4, 10^8]$	0.40(6)	4.31/10	0.56(3)	6.4(11)
					3.82/10

Table 4 Estimate of q_{EA} for three subcritical temperatures, using two different extrapolating functions. For $T = 0.6, 0.8$ both are very good, but at $T = 0.7$ (where we have better statistics) they are somewhat forced. This suggests that the real q_{EA} probably lies in between our two estimates. For the power law extrapolation, Eq. (28), we also quote the exponent B . Notice that this exponent is not proportional to T .

when we tried both extrapolating methods for $T = 0.7$, where we had simulated many more samples, we found that they were somewhat forced. This leads us to conclude that the real asymptotic behavior of $C_\infty(t)$ is probably something in between equations (28) and (29). We shall use the difference between both methods with a fitting window of $t \in [10^3, 10^8]$ as our uncertainty interval,

$$\begin{aligned} 0.62 &\leq q_{\text{EA}}(T = 0.6) \leq 0.733, \\ 0.474 &\leq q_{\text{EA}}(T = 0.7) \leq 0.637, \\ 0.368 &\leq q_{\text{EA}}(T = 0.8) \leq 0.556. \end{aligned} \quad (30)$$

Even with our unprecedently long simulations, we are still at the threshold of being able to compute q_{EA} .

5.2 Energy density and scaling exponents

The time decay of the energy density offers further insights into the connection between statics and dynamics (see Sect. 6). At all temperatures the $L = 80$ energy data are well described by a power-law decay

$$e(t_w) - e_\infty = A t_w^{-\varepsilon(T)}, \quad (31)$$

with e_∞ the asymptotic (equilibrium) energy value. At the critical temperature T_c , general scaling arguments relate the decay exponent ε to the dimension of the energy operator $d_e = (Dv - 1)/v$ and the critical dynamic exponent z [45] :

$$e(t_w; T_c) - e_{\infty; T_c} = A t_w^{-d_e/z_c}. \quad (32)$$

We could then in principle extract $\varepsilon(T_c = 1.1)$ and compare with the best estimate available (considering $v = 2.45$ by Hasenbusch *et al.* [39] and $z_c = z(T_c) = 6.86$ [33] we expect $\varepsilon(T_c) \simeq 0.378$). Unfortunately we do not have enough statistics at the critical temperature to allow for fair fits and statistical accuracy in the determination of the decay exponent, but we can avoid such difficulty. Assuming critical dynamics in all the Spin Glass phase ($T < T_c$) such relation could be extended and tested at all simulated temperatures, provided a T -dependent dynamic exponent $z(T)$ is considered (see Sect. 3 above). In addition, given

T	E_∞	A	ε
0.6	-1.77862(10)	0.122(11)	0.193(6)
0.7	-1.77084(7)	0.148(15)	0.236(7)
0.8	-1.75947(7)	0.155(16)	0.268(7)
0.9	-1.74429(13)	0.19(1)	0.312(5)

Table 5 Results for the power-law decay parameters, Eq. (31).

an inversely proportional dependence of $z(T)$ on the temperature, we expect that $\varepsilon(T) \propto T$. Once the exponent has been determined for some values of $T < T_c$, we can extrapolate to determine $\varepsilon(T_c^-)$. The exponent may be in principle discontinuous at the critical point, so some analysis has been performed also at $T = 1.15$, slightly higher than T_c , to have a hint on the possible value of the right limit $\varepsilon(T_c^+)$.

At all temperatures a fit to power law Eq. (31) is quite sensitive to the fitting window. This is not surprising as the early dynamics may be very different from the asymptotic behavior. In addition, we are aware that our data may suffer from important finite size effects when the coherence length grows up over some fraction of the system size (see [33]). The limit in t_w beyond which data for some observable cannot be considered in the thermodynamic limit depends on temperature and on both the observable and the precision with which it can be measured (which for the energy is very high, of order one part in 10^5). At each temperature, the upper limit in the fitting window should then in principle depend on when, in Monte Carlo time, we start experiencing finite size effects in the energy. We can check this by comparing with the energy decay of systems of size $L = 40$. As an example, in Fig. 16 we report the difference $e_{L=40}(t_w) - e_{L=80}(t_w)$ at $T = 0.8$ as function of t_w : no appreciable deviations appear in the whole simulated range, allowing us to extend our fit to the largest available time. We are then left with adjusting the lower limit t_{\min} by checking that the fit parameters e_∞ , A and ε go to stable values.

Results for ε as function of t_{\min} at all simulated temperatures are depicted in Fig. 17, left. At low temperatures it has been possible to probe for t_{\min} ranging in several decades. At higher T , it is not possible with our data to have fair fits at larger t_{\min} values, as very

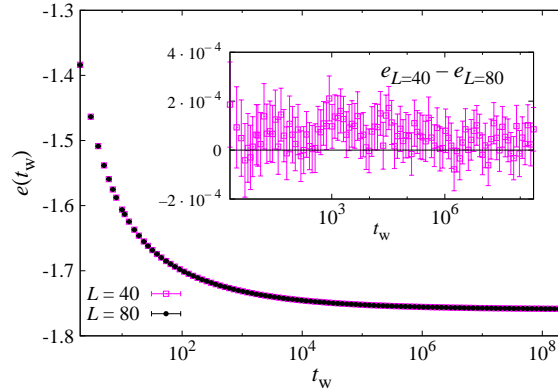


Fig. 16 No appreciable dependence of the decay $e(t_w)$ on the system size, for lattices $L = 40$ and $L = 80$ at $T = 0.8$. **Inset:** the difference between the two as a function of Monte Carlo time.

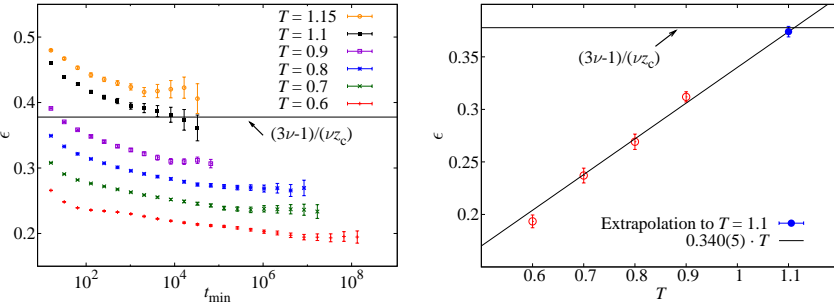


Fig. 17 **Left:** dependence of ϵ on the fitting window. For each choice of the lower limit t_{\min} we fit for all points $t_w > t_{\min}$. We do not assume any upper limit in the fitting window (see text). At lower temperatures we find t_{\min} -independent parameters, with clear plateaus showing up. For each curve the plateau value is taken considering the midpoint in the last longer series of an even number of points lying on an horizontal line within error bars. At $T \geq 1.1$ no clear plateau appears, while large fluctuations spoil the fits. The horizontal line is a prediction for $\epsilon(T_c)$ considering the value of the critical exponent ν of [39] and $z_c = z(T_c) = 6.86$ from Table 2. **Right:** the plateau values for $\epsilon(T)$ for simulated values of $T \leq 0.9$ as function of T (empty circles, red color online). A proportionality law $\epsilon(T) = cT$ works well, and allows one to extrapolate ϵ up to $T_c = 1.1$ (the upper full circle, blue color online). The horizontal line is the best estimate by taking the ν value of [39] and z_c from Table 2.

large fluctuations arise, thus hiding any possible plateau (error bars are from a jackknife procedure).

At $T = 0.6, 0.7, 0.8$ we considered the parameters converged in the last five points in Fig. 17 left; at $T = 0.9$ the last three points converged within error bars. In any of these intervals, we take the mid-point as the plateau values, and report them in the plot of Fig. 17 right (corresponding values of all parameters are reported in Table 5). The data are well represented by a temperature-proportional law, with $\chi^2/\text{d.o.f.} = 4.8/3$. The extrapolated value of $\epsilon(T_c^-)$ is $0.373(5)$ that coincides within errors with the best estimate reported above. This is a quite good *a posteriori* confirmation that the procedure described is robust, leastwise, within the precision attainable. From Fig. 17 left, we see that at $T = 1.1, 1.15$ we were not able to identify a clear plateau and estimate ϵ directly, still there is a trend towards the expected critical value, supporting that $\epsilon(T)$ should be linear up to the critical point at least.

From the values of $\epsilon(T) = (3\nu - 1)/(\nu z(T))$,¹³ we obtain $z(0.6) = 13.4(3)$, $z(0.7) = 11.0(3)$ and $z(0.8) = 9.7(3)$ in agreement with the results of Table 2.

Alternatively we can link these numerical results with an analytical one obtained by Franz *et al.* [46] (see also [48]). In this reference, the contribution of the interface was computed in the framework of Replica Symmetry Breaking. Assuming the power law behavior of the coherence length, one would expect that $\epsilon(T) = 2.5/z(T)$. So, inputting our values for $z(T)$ we obtain $\epsilon(T) = 0.33T$, which is compatible with our numerical finding ($\epsilon(T) = 0.340(5)T$, see Fig. 17 (left)).

We conclude this section by testing in nonequilibrium simulations (see also [47]), the correction-to-scaling exponent measured by Hasenbusch *et al.* [39] $\omega = 1.0$. Our data at $T_c = 1.1$ are well described by a double power-law (for $t_w > 2^6$, $\omega = 1.0$, $\epsilon = 0.378$)

$$e(t_w) - e_\infty = A t_w^{-\epsilon} \left(1 + B t_w^{-\omega/z_c} \right), \quad (33)$$

¹³ The formula is expected to be valid if the value of the exponents below the critical temperature are controlled by their value at T_c .

giving $e_\infty = 1.70201(2)$, $A = 0.149(2)$, $B = 1.25(5)$ and $\chi^2/\text{d.o.f} = 104.20/102$.

5.3 The thermoremanent magnetization

The thermoremanent magnetization of a SG has been known since the 1980s to decay with a power law [49,50] (deviations to this simple behavior were observed only extremely close to T_c , namely $T > 0.98T_c$). As we said in Sect. 2.2, this observable can be identified with $C(t, t_w)$ for fixed t_w and $t \gg t_w$. Following [51], we have fitted our data to a decay law

$$C(t, t_w) = A'(t_w) + B(t_w)t^{c(t_w)}. \quad (34)$$

The constant term $A'(t_w)$ is justified because for a finite number of samples, the correlation function does not go to zero for large times. The very same problem arises in the analysis of experimental data [49] (it was solved by taking a numerical derivative).

We summarize the results of these fits on Table 6. We fixed $t_w = 2, 4, 8, 16$ and fitted our data up to the point where finite size effects appear ($t < 2 \times 10^{10}$ for $T = 0.7$, $t < 4 \times 10^8$ for $T = 0.8$ and the whole range for $T = 0.6$). We started our fits at $t = 10^6$, but this limit can be varied along several orders of magnitude with no change in the fitting parameters or the goodness of the fit. As we can see, the exponent c has a slight, but systematic, dependence on t_w . This tendency was already observed by [23].

Our estimates for c can be compared with experimental values [49]

$$\begin{aligned} c(T = 0.55T_c) &\approx -0.12, \\ c(T = 0.67T_c) &\approx -0.14, \\ c(T = 0.78T_c) &\approx -0.17, \end{aligned} \quad (35)$$

(the error bars on these exponents are small, not much larger than the size of the plotted data points in Fig. 3b of [49]). When compared with the values in Table 6, the experimental exponents are similar but slightly higher (let us recall that $0.6 \approx 0.55T_c$, $0.7 \approx 0.64T_c$ and $0.8 \approx 0.73T_c$).

A different approach comes from realizing that in experimental work t and t_w typically differ by at most 4 orders of magnitude, while in our fits they differ by as many as 9 or 10.

T	t_w	t_{\min}	$c(t_w)$	$d(t_w)$	$A'(t_w) \times 10^3$	$\chi^2/\text{d.o.f.}$
0.6	2	10^6	-0.1525(23)	2.14(5)	2.6(6)	14.7/64
	4	10^6	-0.1495(22)	2.10(5)	2.8(8)	15.5/64
	8	10^6	-0.1459(20)	2.05(4)	2.5(10)	17.4/64
	16	10^6	-0.1430(19)	2.01(4)	2.4(12)	17.5/64
0.7	2	10^6	-0.1787(14)	2.067(27)	1.47(25)	23.3/50
	4	10^6	-0.1765(13)	2.041(26)	1.8(3)	18.4/50
	8	10^6	-0.1733(12)	2.004(25)	1.7(4)	18.9/50
	16	10^6	-0.1704(12)	1.971(25)	1.6(5)	15.4/50
0.8	2	10^6	-0.210(8)	1.98(9)	1.7(10)	13.9/32
	4	10^6	-0.212(7)	2.00(8)	2.8(12)	11.1/32
	8	10^6	-0.208(7)	1.96(8)	3.0(14)	10.8/32
	16	10^6	-0.205(6)	1.93(7)	3.0(18)	8.43/32

Table 6 Exponents c and d and parameter A' of equations (34) and (38). The values of c come from fits, whose χ^2 we also show. The exponent d comes from $d = -cz$, where z is the dynamic exponent of equation (22) and Table 2. Fits are limited to the time range where the system is free of finite size effects, which accounts for the different numbers of degrees of freedom for each temperature.

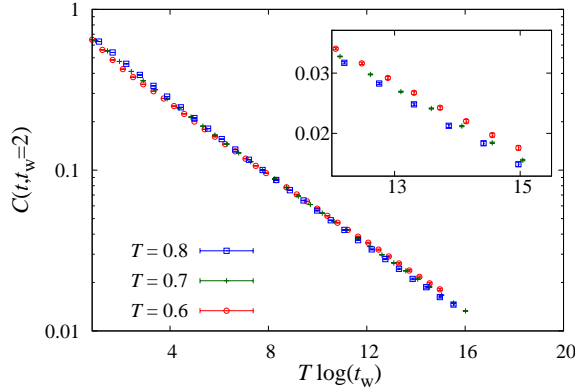


Fig. 18 $C(t, t_w = 2)$ as a function of $T \log(t)$ for three subcritical temperatures. The inset shows that the scaling holds only approximately.

Taking this into account, it is interesting to consider a power law where the fitting window is shifted with t_w so that $1 \leq t/t_w \leq 10$ [33],

$$C(t, t_w) = A(t_w) (1 + t/t_w)^{-1/\alpha(t_w)}. \quad (36)$$

Using this functional form and extrapolating $-1/\alpha(t_w)$ to a typical experimental time with a quadratic fit we obtain

$$\begin{aligned} -1/\alpha(t_w = 100 \text{ s}) &\approx -0.11, & T = 0.6 &\approx 0.55T_c, \\ -1/\alpha(t_w = 100 \text{ s}) &\approx -0.12, & T = 0.7 &\approx 0.64T_c, \\ -1/\alpha(t_w = 100 \text{ s}) &\approx -0.14, & T = 0.8 &\approx 0.73T_c. \end{aligned} \quad (37)$$

These extrapolations are slightly above the experimental values of equation (35), but if both sets of exponents are interpolated with a parabola, the two curves result roughly parallel, i.e., our extrapolation error seems temperature-independent.

Since both the thermoremanent magnetization, Eq. (34), and the coherence length are well described by a power law, it follows that $C(t, t_w)$ should be a power of $\xi(t + t_w)$, at least for the small values of t_w in Table 6,

$$C(t, t_w) \sim \xi(t + t_w)^{-d}. \quad (38)$$

Indeed, following the same procedure we used for the exponent a of equation (13) (see Sect. 3.2) we have computed the values of d for $t_w = 2, 4, 8, 16$ (Table 6), obtaining $d \approx 2$. Incidentally, let us remark that the coherence length is notoriously difficult to access experimentally [5], while the thermoremanent magnetization is a pretty standard measurement. Eq. (38) then appears as an interesting, albeit indirect, way of estimating experimentally an effective coherence length.

Notice that the exponents $c(t_w)$ of Table 6 are roughly, but not exactly, linear in T . This suggests that the thermoremanent magnetization should be a temperature-independent function of $T \log(t)$ [50]. Fig. 18 shows that this is only an approximate claim.

T	t_w	t_{\min}	$e(t_w)$	$f(t_w)$	$\chi^2/\text{d.o.f.}$
0.6	2	10^3	-0.236(7)	0.873(9)	52.2/104
		10^6	-0.30(6)	0.82(5)	13.9/64
	4	10^3	-0.203(6)	0.909(8)	47.9/104
		10^6	-0.25(4)	0.85(4)	13.5/64
	8	10^3	-0.176(4)	0.943(7)	41.5/104
		10^6	-0.21(3)	0.90(4)	13.9/64
	16	10^3	-0.158(4)	0.968(7)	38.1/104
		10^6	-0.19(3)	0.92(4)	15.3/64
	0.7	10^3	-0.263(4)	0.890(4)	43.0/90
		10^6	-0.32(3)	0.84(3)	14.4/50
		10^3	-0.230(3)	0.921(4)	71.9/90
		10^6	-0.29(3)	0.862(25)	12.8/50
		10^3	-0.2003(23)	0.955(3)	94.1/90
		10^6	-0.253(23)	0.895(23)	13.0/50
		10^3	-0.1768(20)	0.985(3)	138/90
		10^6	-0.226(19)	0.921(22)	10.6/50
		10^3	-0.302(16)	0.891(16)	45.1/72
0.8	2	10^6	-0.5(3)	0.77(15)	14.3/32
		10^3	-0.257(12)	0.934(14)	63.6/72
	4	10^6	-0.6(4)	0.71(17)	11.4/32
		10^3	-0.223(10)	0.970(13)	69.8/72
	8	10^6	-0.49(24)	0.76(12)	11.1/32
		10^3	-0.192(8)	1.008(12)	65.9/72
	16	10^6	-0.40(19)	0.81(12)	8.49/32

Table 7 Parameters of a fit to Eq. (39), offering an alternative description of the thermoremanent magnetization. For each temperature, the maximum time included in the fit was such that $\xi(t_{\max}) = 10$.

The incompatibility of the values in Eqs. (35) and (37), together with the fact that we needed the constant term $A'(t_w)$ in (34), suggests that there probably exists a systematic error in the power law fits of Table (6).¹⁴ One may consider an alternative description,

$$C(t, t_w) = A''(t_w) \exp \left[e(t_w) (\log t)^{f(t_w)} \right], \quad (39)$$

that would reproduce a power law if $f(t_w) = 1$. Eq. (39) should not be confused with the stretched exponential, discarded in reference [49] for all T but the closest to T_c . We show our results for this fit in Table 7. From the point of view of a χ^2 test, the two descriptions, (34) and (39), are equally good. The fit parameters are remarkably stable with variations of the fitting window. As we see, the values of $f(t_w)$ are very close to, but incompatible with, 1 (at least for the lowest temperatures).

Let us conclude this section by considering again the effects of statistical data correlation on fit parameters. Specifically, let us consider the exponent $\alpha(t_w)$ of equation (36), see Fig. 19 and reference [33]. The alert reader will notice strange wiggles, large as compared with the error bars, which are specially prominent for the fit with 63 samples. The reason is that data for different t and t_w in this fit are even more correlated than usual. In fact, we have sampled the function $C(t, t_w)$ for t and t_w integer approximations to $2^{i/4}$, $i = 0, 1, \dots$. For each t_w , we perform the fit and extract $\alpha(t_w)$ for $t_w \leq t < 10t_w$. In other words, for each t_w we used 14 values of t . Recall that the spin configurations involved are the one at time t_w , and the 14 spin configurations at succeeding times $t + t_w$. Given our choice for integer t

¹⁴ Note, however, that the smallest value of $C(t, t_w = 2)$ that we reach is ~ 0.013 , pretty large as compared with $A'(t_w)$.

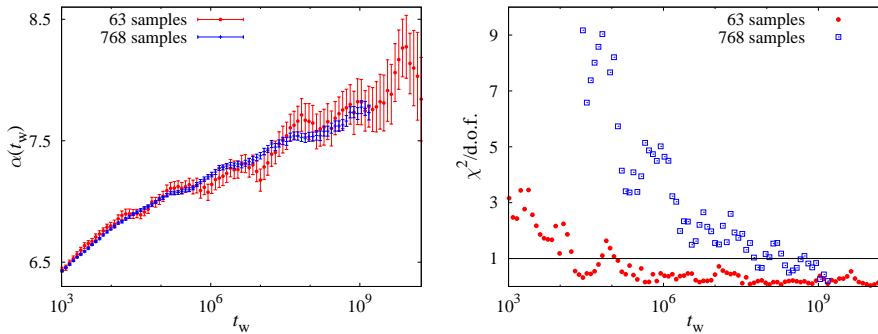


Fig. 19 Exponent $\alpha(t_w)$ defined in equation (36) as a function of t_w at $T = 0.7$, computed for the 63 samples of [33] and for our 768 samples. The right panel shows the values of diagonal χ^2 for both fits.

and t_w , it follows that, for the next t_w , in the computation of C we will use 13 out of the 14 spin configurations used at the earliest t_w . For the second-next t_w , the number of repeated configurations will be 12, and so forth. This is the origin of the dramatic data correlation: the very same spin configurations are being used for consecutive times. Notice that when the statistics is increased to 768 samples, the period of these oscillations does not change, but their amplitude decreases. Also in Fig. 19, right panel, we show the value of $\chi^2/\text{d.o.f.}$ for the fits with 63 and 768 samples. In both cases, χ^2 decreases strongly with t_w , but, while the fit with 63 samples was perfectly reasonable from $t_w \sim 10^4$, that with 768 samples is not good until $t_w \sim 10^8$. The increased accuracy reveals systematic deviations from equation (36). Nevertheless, the estimate of $\alpha(t_w)$ for both fits is compatible in a much wider range.

5.4 C_{link} as a function of C^2

Studying C_{link} as a function of C^2 for fixed t_w we can monitor the scaling of the active domains' surface area. This scaling has an exact correlate in equilibrium studies [52], where one considers the probability distribution function of

$$Q_{\text{link}} = \frac{1}{ND} \sum_{\langle \mathbf{x}, \mathbf{y} \rangle} \sigma_x^{(1)} \sigma_x^{(2)} \sigma_y^{(1)} \sigma_y^{(2)}. \quad (40)$$

The analogue of C_{link} as a function of C^2 is the conditional expectation value $\langle Q_{\text{link}} | q^2 \rangle$. Indeed, in [33], we quantitatively compared our dynamical results with the equilibrium $\langle Q_{\text{link}} | q^2 \rangle$ of [52]. It was found that a convenient time-length dictionary could be established in such a way that the equilibrium results for finite lattices reproduced the nonequilibrium results for finite $\xi(t_w)$. For instance, for $T = 0.7$, when $L/\xi(t_w) \approx 3.7$, $C_{\text{link}}(C^2, t_w) \simeq \langle Q_{\text{link}} | q^2 \rangle_L$.

In [33] it was found that C_{link} is a smooth increasing function of C^2 at least up to experimental scales. On the other hand, for systems undergoing coarsening dynamics (e.g., a disordered ferromagnet), C_{link} tends to a constant C^2 -independent value whenever $C^2 < q_{\text{EA}}^2$. Let us briefly justify these expectations.

On the one hand, since in the RSB scenario the coherent domains are not compact objects, one would expect C_{link} to have the same aging properties as C^2 , that is, dC_{link}/dC^2

should not vanish. This is the nonequilibrium analogue of the overlap equivalence property [52]. For instance, in the Sherrington-Kirkpatrick model it is straightforward to show that $C_{\text{link}} = C^2$.

On the other hand, to find the scaling for a coarsening image of compact active droplets we need a more elaborate argument. We consider a large droplet of size $\xi(t+t_w)$ at time $t+t_w$ that, at time t_w , was made of N_C smaller droplets of size $\xi(t_w)$. The number of spins in the boundary of a droplet at time t_w scales as $\xi(t_w)^{D_s}$. Typically, $D_s = D - 1$, but one may have $D - 1 \leq D_s \leq D$ [6, 16] (for the TNT model of SG, $D - D_s \approx 0.45$ for $D = 3$, see [55] and Palassini and Young in [18]). Of course, N_C scales as $N_C \sim [\xi(t+t_w)/\xi(t_w)]^D$. The overlap of each of the N_C droplets at time t_w with the configuration at time $t+t_w$ is randomly $\pm q_{\text{EA}}$. Hence, the scaling of $C(t, t_w)$ is, for the region $C < q_{\text{EA}}$,¹⁵

$$C(t, t_w) \sim \sqrt{N_C} \left(\frac{\xi(t_w)}{\xi(t+t_w)} \right)^D \sim \left(\frac{\xi(t_w)}{\xi(t+t_w)} \right)^{D/2}. \quad (41)$$

Now, for the link overlap we expect (C_{link}^0 is the equilibrium expectation value of Q_{link})

$$C_{\text{link}}(t, t_w) = C_{\text{link}}^0 + N_C \frac{\xi^{D_s}(t_w)}{\xi^D(t+t_w)}. \quad (42)$$

In fact, the decay of $C_{\text{link}}(t, t_w)$ comes mainly from the contribution of droplets' surface at time t_w . In particular, for $t \rightarrow \infty$, the excess of C_{link} over C_{link}^0 is just the probability that a link belongs to the surface of a droplet at time t_w . Now, considering equation (41) we conclude that the number of droplets N_C scales with $C(t, t_w)$ as

$$N_C \sim \frac{g(C)}{C^2}, \quad (43)$$

where the function $g(C)$ is continuous, but not necessarily differentiable at $C = 0$, and where $g(0) > 0$. Combining Eq. (43) and Eq. (41) we get

$$C_{\text{link}}(t, t_w) = C_{\text{link}}^0 + C_{\text{link}}^1 g(C) \xi^{D_s-D}(t_w). \quad (44)$$

In the above expression C_{link}^1 is a constant. Notice that, in particular, equation (44) implies that the derivative of C_{link} with respect to C^2 goes to zero as $t_w \rightarrow \infty$.

We can easily check Eq. (44) for the two-dimensional Ising model, where the Onsager and Yang solutions provide exact values for C_{link}^0 and q_{EA} (in this case $D - D_s = 1$). As for the growth of the coherence length, it scales as $t_w^{1/2}$ (see, for instance [53]). As expected, see Fig. 20, C_{link} tends to a constant function $C_{\text{link}}(C, t_w \rightarrow \infty) = C_{\text{link}}^0$ for $C < q_{\text{EA}}$. As we show in Fig. 20, right, the approach to this constant is well described by Eq. (44).

As for the Edwards-Anderson model, C_{link} is seen to be a very smooth function of C^2 [33], so we can easily compute the curve $C_{\text{link}}(C^2 = 0, t_w)$ with a linear extrapolation. We can also study $C_4(r = 1, t_w)$, which is the nonequilibrium disorder average of $Q_{\text{link}}(t_w)$, Eq. (40). The two curves are plotted against $\xi^{-1}(t_w)$ and $\xi^{-0.45}(t_w)$ in Fig. 21. In accordance with the previous discussion, and in particular with the relation $C_{\text{link}}(C^2 = 0, t_w(L)) = \langle Q_{\text{link}} | q^2 = 0 \rangle_L$, both have the same extrapolation to infinite time (they actually collapse on the same curve for large times). Of the two, the ξ^{-1} scaling is more convincing.

¹⁵ Even if Eq. (41) is intuitively evident, it can be backed by an explicit computation. From Eq. (6-11) in [54], one easily shows for the *Ising* ferromagnet that the spin-spin correlation function takes the form of a series $C(t, t_w) = a_1 y + a_2 y^2 + \dots$, where $y = \xi^{D/2}(t+t_w) \xi^{D/2}(t_w) / [\xi^2(t+t_w) + \xi^2(t_w)]^{D/2}$. Eq. (41) follows when $\xi(t+t_w) \gg \xi(t_w)$.

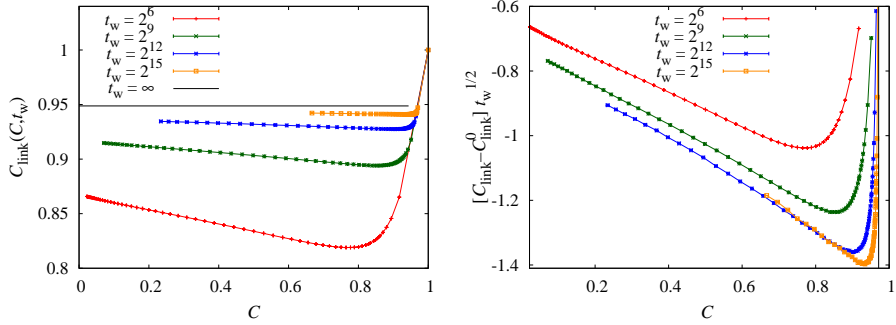


Fig. 20 **Left:** C_{link} as a function of C for the two-dimensional ferromagnetic Ising model at $T = 0.66T_c$. Results obtained for an $L = 4096$ lattice (the results were averaged over 20 trajectories). **Right:** Numerical check of Eq. (44) for the data on the left panel. The vertical line is at $C = q_{\text{EA}}$. We see that, for large t_w and $C < q_{\text{EA}}$, $C_{\text{link}}(C, t_w) - C_{\text{link}}^0$ scales as ξ^{-1} .

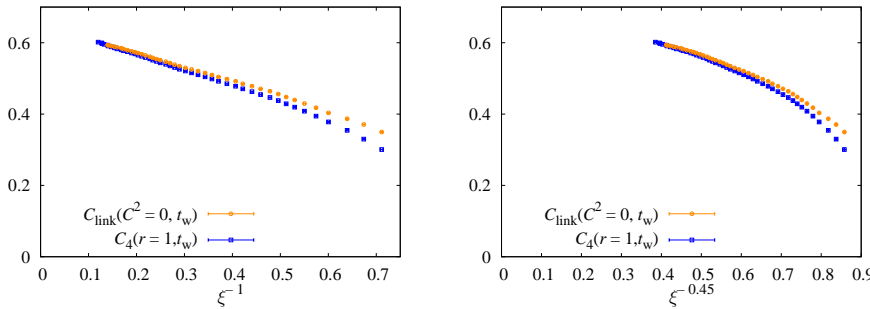


Fig. 21 Extrapolation of $C_{\text{link}}(C^2, t_w)$ to $C^2 = 0$, together with $C_4(r = 0, t_w)$, against $\xi_{1,2}^{-1}(t_w)$ (**Left**) and $\xi_{1,2}^{-0.45}(t_w)$ (**Right**) (plot for our 96 samples at $T = 0.6$).

Equation (44) suggests plotting $dC_{\text{link}}(C^2, t_w)/dC^2$ (see [33] for details) against $\xi^{-1}(t_w)$ (Fig. 22, left) and against $\xi^{-0.45}(t_w)$ (Fig. 22, right). It is important to choose a value C_*^2 of C^2 smaller than q_{EA}^2 but not too small, because otherwise the numerical estimate for the derivative would be unreliable. We have used the most pessimistically small estimates of q_{EA}^2 in Table 4. The two representations are linear within our errors. However, while a $\xi^{-1}(t_w)$ scaling compatible with standard coarsening seems falsified (the extrapolation to infinite time is well above zero), a $\xi^{-0.45}(t_w)$ scaling towards zero is compatible with our data.

From Fig. 21 and Eq. (44), we conclude that the difference $C_{\text{link}}(C^2, t_w) - C_4(r = 1, t_w)$ should vanish as $\xi^{D_s-D}(t_w)$ in a coarsening system. We show this difference in Fig. 23, for the same fixed value C_*^2 we used for the derivative. As we see, the extrapolation as ξ^{-1} is smooth and positive. On the other hand, the $\xi^{-0.45}$ scaling could only be possible if our whole simulation were in a pre-asymptotic regime.

This discussion notwithstanding, two comments are in order. First, equation (44) relies on equation (41), which is disproved by the values of exponent d in Table 6 (we obtain $d \approx 2$, rather than $d = 3/2$). Second, we mark by crosses in Fig. 22 the experimentally relevant scale: the derivative is certainly nonvanishing there in either case.

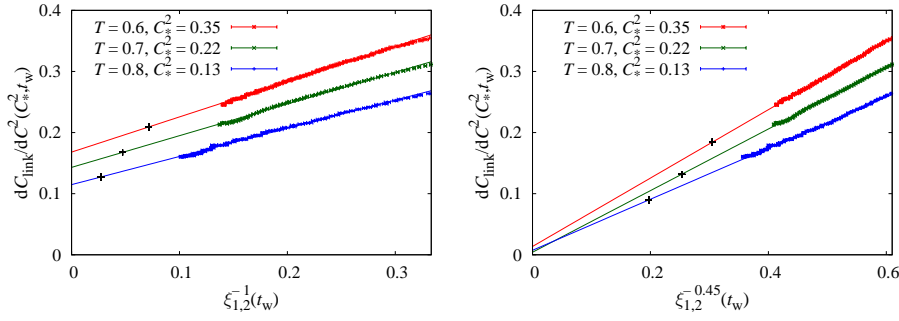


Fig. 22 Derivative of $C_{\text{link}}(C^2, t_w)$ with respect to C^2 versus $\xi_{1,2}^{-1}(t_w)$ (**Left**) and versus $\xi_{1,2}^{-0.45}(t_w)$ (**Right**) for three subcritical temperatures ($T = 0.6, 0.7, 0.8$, from top to bottom). Lines are linear least squares fits. We mark by crosses our extrapolations for the experimental scale of ξ ($t_w = 100$ s). The curves are plotted for a fixed value $C^2 = C_*$, chosen to be just below our lower bound for q_{EA} at each temperature from Eq. (30).

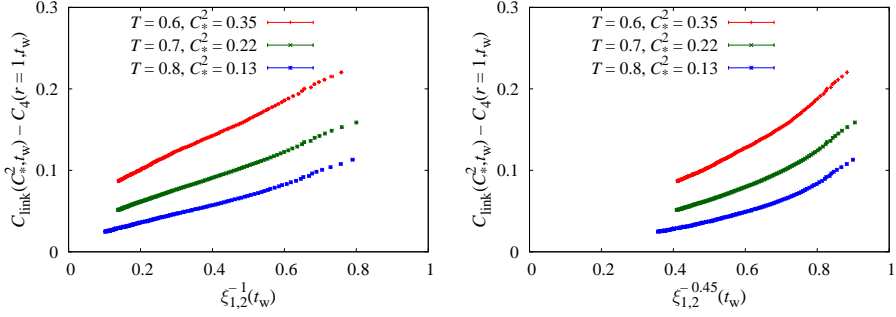


Fig. 23 Difference $C_{\text{link}}(C^2, t_w) - C_4(r = 1, t_w)$ for the same C_*^2 of Fig. 22. The curves are plotted against $\xi_{1,2}^{-1}(t_w)$ (**Left**) and against $\xi_{1,2}^{-0.45}(t_w)$ (**Right**). An extrapolation to zero seems unlikely even for the $\xi_{1,2}^{-0.45}$ case.

6 Scaling of the dynamical coherence length

As we have shown in Table 2, our data for the coherence length is very well represented by a power law in t_w . We found an exponent $z(T)$ roughly linear in T^{-1} . Some theoretical grounds for this behavior can be found in [51, 56]. It also appears in the numerical simulation of the Sherrington-Kirkpatrick model [57]. Nevertheless, an alternative interpretation has been suggested [12]. We now reanalyze our data under this light.

6.1 Mixed scaling

The Saclay group proposed [12], see also [9], a mixed scaling for the dynamical coherence length, which assumes both critical behavior and activated dynamics in a wide range of temperatures in the glassy region:

$$t_w \sim \tau_0 \xi^{z_c} \exp\left(\frac{Y(T)\xi^\psi}{T}\right), \quad (45)$$

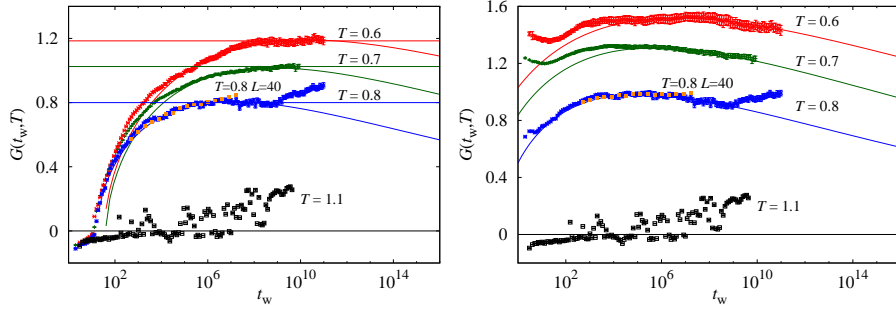


Fig. 24 **Left:** Function $G(t_w, T)$ defined in Eq. (46) versus t_w , for $T = T_c = 1.1$, $T = 0.8$, $T = 0.7$ and $T = 0.6$. Our estimates for the plateau (see text) are indicated with horizontal lines. The continuous curves are $G(t_w, T)$ as computed from (48), fixing $\tau_0(T) = \tau_0(T_c)$, using $z(T)$ computed in the power law fits of Table 2. At $T = 0.8$ we also show our data for $L = 40$. **Right:** As in left panel, but now we allow τ_0 to depend on T , Eq. (49).

where τ_0 is the microscopical time associated to the dynamics; z_c is the dynamical critical exponent computed at the critical point; ψ is the exponent that takes the free energy barriers into account (from the dynamical point of view) and $Y(T) = Y_0(1 - T/T_c)^{\psi\nu}$, with the ν exponent being the static critical exponent linked to the coherence length. Near the critical point $Y(T) \rightarrow 0$ and the power law critical dynamics is recovered.

To assess the validity of the mixed scaling hypothesis, we consider the following function [12]:

$$G(t_w, T) = \left(\frac{\log(t_w/\tau_0) - z_c \log \xi(t_w, T)}{\xi^\psi T_c / T} \right)^{\frac{1}{\psi\nu}}. \quad (46)$$

Equation (45) would imply that $G(t_w, T)$ is a t_w -independent function of temperature,

$$G(t_w, T) = G_0 \left[1 - \frac{T}{T_c} \right], \quad (47)$$

where $G_0 = (Y_0/T_c)^{1/(\psi\nu)}$. Both the Ising and Heisenberg experimental samples¹⁶ behave consistently with this expectation. In this study, the parameters were taken to be $z_c = 5$ and $\psi = 1.5$ (those of AgMn, a Heisenberg SG) [12].

Notice that $G(t_w, T)$ would be exactly zero if ξ followed a pure power law with z and τ_0 fixed to their critical temperature values,

$$\xi(t_w) = \left[\frac{t_w}{\tau_0(T_c)} \right]^{1/z(T_c)}, \quad (48)$$

In the case of a power law with parameters τ and z different from those computed at the critical point, we expect that the function $G(t_w, T)$ should be zero only for $t_w \rightarrow \infty$. In order to avoid a painful and somewhat arbitrary fit, we take the relevant parameters in Eq. (46) from the literature (z and τ_0 are taken at T_c): $T_c = 1.109$ [39], $\psi \simeq 0.7$ [23], $z_c = 6.86$ [33] and $\nu = 2.45$ [39].

In Fig. 24 left, we show the function $G(t_w, T)$ for four values of the temperature (including T_c). Although $G(t_w, T)$ is not t_w -independent, it plateaus at a value $G_a(T)$ for long times.

¹⁶ Ag:Mn at 2.5% (Heisenberg like), CdCr_{1.7}IN_{0.3}S₄ (also Heisenberg like) and Fe_{0.5}Mn_{0.5}TiO₃ (Ising like).

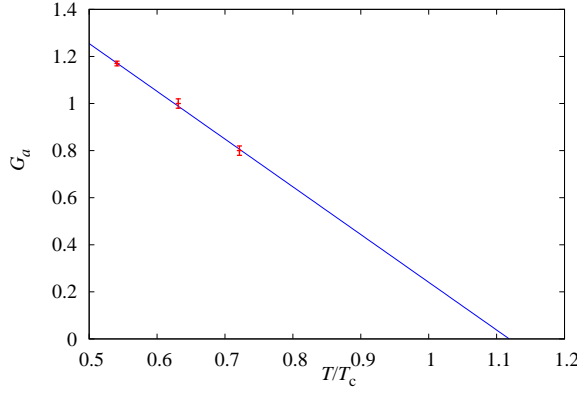


Fig. 25 The plateaus $G_a(T)$ in Fig. 24 against T/T_c . The line is a linear fit ($\chi^2/\text{d.o.f.} = 0.12/1$), that extrapolates to zero at $T/T_c = 1.12(21)$, which is compatible with one.

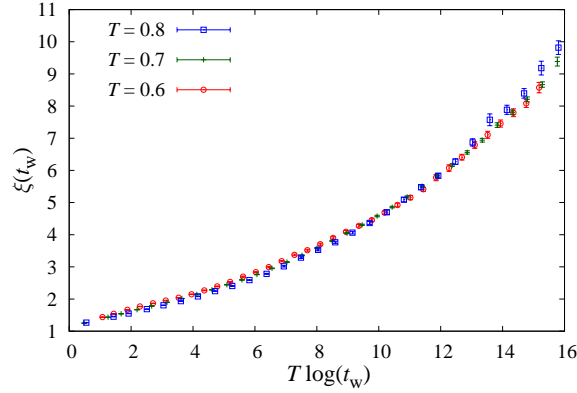


Fig. 26 Coherence length $\xi_{1,2}(t_w)$ as a function of $T \log t_w$, for three subcritical temperatures. Even if the three curves are not equal within errors, the overall scaling is suggestive.

This is especially clear for $T = 0.6$ and $T = 0.8$, while at T_c we expect it to be compatible with zero. For $T = 0.7$ the plateau is not well defined, but we estimate it as the average of the last points¹⁷. As we show in Fig. 25, $G_a(T)$ behaves consistently with Eq. (47). Hence, we are in a time region where experimental results for $G(t_w, T)$ are reproduced.

However, we will remark the following points:

1. The departure of the curve for $T = 0.8$ from the plateau in Fig. 24 is a finite size effect, as shown explicitly by our $L = 40$ data (see also [33]). A similar, though milder, effect afflicts the data for $T = 0.7$ for $t_w > 2.2 \times 10^{10}$. The same effect is very clear at T_c , for even shorter times.

¹⁷ In order to assign error bars to the plateau values, we consider only the biggest contributions, those from the uncertainties in z_c and in $\tau_0(T_c)$.

2. Were $\xi(t_w)$ a power law, the curve for $G(t_w, T)$ would be decreasing (for larger times). On the other hand, we know that finite size effects cause it to increase. The plateau may well be an artificial combination of these two effects.

To clear up this problem, we also show in Fig. 24, right, the value of $G(t_w, T)$ computed using the coherence length and $\tau_0(T)$ from a fit to

$$\xi(t_w) = \left[\frac{t_w}{\tau_0(T)} \right]^{1/z(T)}. \quad (49)$$

Note that, at variance with Eq.(48), we now allow τ_0 to depend on T . These fits were reported in Table 2. Specifically, we obtained $\tau_0(T = 0.6) = 0.008(3)$, $\tau_0(T = 0.7) = 0.030(8)$, $\tau_0(T = 0.8) = 0.17(4)$ and $\tau_0(T_c) = 0.58(13)$.¹⁸

Although the physical meanings of Eqs. (46) and (49) are quite different, the two of them account fairly well for our data.

However, Eq. (49) describes well the data in nearly the whole range of times (actually for $\xi \gtrsim 3$) while Eq. (46) describes the data only in the region where the right hand side of Eq. (46), computed with Eq. (48), is nearly constant. Moreover the data for $\xi(t_w)$ nearly collapse if we use the variable $T \log t_w$, see Fig. 26. This collapse is not compatible with Eq. (45). Henceforth, the activated scaling hypothesis, Eq. (45), implies that our data are entirely in a pre-asymptotic regime. We note nevertheless that extrapolating our data with Eq. (49) to the relevant experimental scale ($t_w = 10^{14}$ or 100 seconds) produces fairly sensible results [33].

7 Conclusions

Using the dedicated computer Janus, we have studied the nonequilibrium dynamics of the Ising spin glass for times spanning eleven orders of magnitude. We have looked into quantities not considered in our previous work [33] and extended the simulations described therein by considering more temperatures and vastly enlarging the number of samples for $T = 0.7$. The emerging picture is that of non-coarsening dynamics.

We have performed an extensive investigation of heterogeneous dynamics, by considering the two-time, two-site correlation function $C_{2+2}(\mathbf{r}, t, t_w)$. We have obtained the first reliable determination of the nonequilibrium correlation length and the exponent for the algebraic decay of C_{2+2} . When t is much smaller than t_w , the correlation length reaches a t_w -independent limit. On the other hand, for t much larger than t_w , the correlation length scales as the coherence length. Thus, it might be sensible to exchange the role of both length scales in the study of structural glasses [42], where a notion of a coherence length is lacking.

Crucial to the above findings has been our integral determinations of characteristic length scales. We have also used them to obtain the coherence length and to study the replicon mode. Indeed, the exponent a in Eq. (13) is definitively nonvanishing, and hence incompatible with the droplets picture. We have also considered nonequilibrium overlap equivalence, with the help of the coherence length.

We have used both the coherence and correlation lengths to obtain safe bounds for the Edwards-Anderson order parameter below the critical temperature.

¹⁸ We have found a monotonic (decreasing) behavior for the microscopic time just as in Ising samples ($\text{Fe}_{0.5}\text{Mn}_{0.5}\text{TiO}_3$) [58]. However, Heisenberg samples have no such clear pattern: $\text{CdCr}_{1.7}\text{IN}_{0.3}\text{S}_4$ shows decreasing monotonic behavior but Ag:Mn at 2.5% and Cu:Mn at 6% [5] present an increasing monotonic one.

As for the thermoremanent magnetization, good agreement with experimental determinations of the temperature-dependent decay exponents have been obtained. A potentially useful observation for experimental work is that the thermoremanent magnetization scales with the coherence length, which is much harder to measure. We also observed that a non power law function could fit the thermoremanent magnetization equally well.

The energy relaxation is well described by a power law. The exponents displayed a nearly linear dependence on temperature. It has been possible to extrapolate to the critical point, finding results in nice agreement with the latest determinations [33,39].

We have shown that the link overlap correlation function C_{link} offers a wealth of information on interphase behavior. Our results have been equally compatible with the droplets and RSB pictures. However, in the droplets picture the scaling with the coherence length of the thermoremanent magnetization is incompatible with our data. Furthermore, irrespective of what happens for infinite time, the variation of C_{link} with C^2 is nontrivial at experimental time scales. This means that the physical view conveyed by the RSB theory is a better representation of the physics at the scale of a few hours.

We have critically examined the time growth of the coherence length, comparing critical and activated dynamics. We have found that both theories describe its behavior equally well.

Finally, we have taken the occasion to give full details of our analysis methods, some of which are quite new.

Acknowledgements We are thankful to P. Nordblad for providing details on the exponents for thermoremanent magnetization decay.

Janus was supported by EU FEDER funds, with reference No. UNZA05-33-003 (MEC-DGA, Spain). Janus was developed in collaboration with ETHlab. We were partially supported by MEC (Spain), through contracts No. FIS2006-08533, FIS2007-60977, FIS2008-01323, TEC2007-64188; from CAM, contract no. CCG07-UCM/ESP-2532 (Spain) and from the Microsoft Prize 2007. D. Yllanes acknowledges support from the FPU program, reference no. AP2007-01149.

References

1. Mydosh, J. A.: Spin Glasses: an Experimental Introduction, Taylor and Francis, London (1993).
2. Vicent E., Hammann, J., Ocio, M., Bouchaud, J.-P., Cugliandolo, L.F.: Slow dynamics and aging in spin glasses. In Rubí, M., and Pérez-Vicente, C. (eds.), Complex Behavior of Glassy Systems, Lecture Notes in Physics **492**, Springer (1996).
3. Rodriguez, G.F., Kenning, G.G., Orbach, R.: Phys. Rev. Lett. **91**, 037203 (2003).
4. Dupuis, V., Bert, F., Bouchaud, J.-P., Hamman, J., Ladieu, F., Parker, D., Vincent, E.: Pramana J. of Phys. **64**, 1109 (2005).
5. Joh, Y.G., Orbach, R., Wood, G.G., Hammann, J., Vincent, E.: Phys. Rev. Lett. **82**, 438 (1999).
6. Fisher, D.S., Huse, D.A.: Phys. Rev. B **38**, 373 (1988).
7. Jonason, K., Vincent, E., Hammann, J., Bouchaud, J.-P., Nordblad, P.: Phys. Rev. Lett. **81**, 3243 (1998); Lundgren, L., Svendlinsh, P., Beckman, O.: Journal of Magn. Magn. Mat. **31-34**, 1349 (1983); Jonsson, T., Jonason, K., Jönsson, P., Nordblad, P.: Phys. Rev. B **59**, 8770(1999); Hammann, J., Vincent, E., Dupuis, V., Alba, M., Ocio, M., Bouchaud, J.-P.: J. Phys. Soc. Jpn. **69**, (2000) Suppl. A, 206-211.
8. Bert, F., Dupuis, V., Vincent, E., Hammann, J., Bouchaud, J.-P.: Phys. Rev. Lett. **92**, 167203 (2004).
9. Berthier, L., Bouchaud, J.-P.: Phys. Rev. B **66**, 054404 (2002).
10. Jimenez, S., Martin-Mayor, V., Perez-Gaviro, S.: Phys. Rev. B **72**, 054417 (2005).
11. Marinari, E., Parisi, G., Ricci-Tersenghi, F., Ruiz-Lorenzo, J.J.: J. Phys. A **33**, 2373 (2000).
12. Bouchaud, J.-P., Dupuis, V., Hammann, J., Vincent, E., Phys. Rev. B **65**, 024439 (2001).
13. Gunnarsson, K., Svedlindh, P., Nordblad, P., Lundgren, L., Aruga, H., Ito, A.: Phys. Rev. B **43**, 8199 (1991).
14. Ballesteros, H.G., Cruz, A., Fernandez, L.A., Martin-Mayor, V., Pech, J., Ruiz-Lorenzo, J.J., Tarancón, A., Tellez, P., Ullod, C.L., Ungil, C.: Phys. Rev. B **62**, 14237 (2000).
15. Palassini, M., Caracciolo, S.: Phys. Rev. Lett. **82**, 5128 (1999).

16. McMillan, W.L.: *J. Phys. C* **17**, 3179 (1984); Bray, A.J., Moore, M.A.: Scaling theory of the ordered phase of spin glasses. In van Hemmen, J.L., Morgenstern, I. (eds.) Heidelberg Colloquium on Glassy Dynamics, Lecture Notes in Physics **275**, Springer, Berlin (1987). Fisher, D.S., Huse, D.A.: *Phys. Rev. Lett.* **56**, 1601 (1986) and *Phys. Rev. B* **38**, 386 (1988).
17. Marinari, E., Parisi, G., Ricci-Tersenghi, F., Ruiz-Lorenzo, J.J., Zuliani, F.: *J. Stat. Phys.* **98**, 973 (2000).
18. Krzakala, F., Martin, O.C.: *Phys. Rev. Lett.* **85**, 3013 (2000); Palassini, M., Young, A.P.: *Phys. Rev. Lett.* **85**, 3017 (2000).
19. Franz, S., Mézard, M., Parisi, G., Peliti, L.: *Phys. Rev. Lett.* **81**, 1758 (1998); *J. Stat. Phys.* **97**, 459 (1999).
20. Parisi, G., Ricci-Tersenghi, F.: *J. Phys. A: Math. Gen.* **33**, 113 (2000).
21. Contucci, P., Giardina, C.: *J. Stat. Phys.* **126**, 917 (2007); *Ann. Henri Poincaré* **6**, 915 (2005).
22. De Dominicis, C., Kondor, I., Temesvári, T.: Beyond the Sherrington-Kirkpatrick model. In Young, A.P. (ed.) Spin Glasses and Random Fields, World Scientific, Singapore (1997).
23. Kisker, J., Santen, L., Schreckenberg, M., Rieger, H.: *Phys. Rev. B* **53**, 6418 (1996).
24. Rieger, H.: *J. Phys. A* **26**, L615 (1993).
25. Jimenez, S., Martin-Mayor, V., Parisi, G., Tarancón, A.: *J. Phys. A: Math. and Gen.* **36**, 10755 (2003).
26. Perez Gaviro, S., Ruiz-Lorenzo, J.J., Tarancón, A.: *J. Phys. A: Math. Gen.* **39** (2006) 8567-8577.
27. Castillo, H.E., Chamon, C., Cugliandolo, L.F., Kennett, M.P.: *Phys. Rev. Lett.* **88**, 237201 (2002); Castillo H.E., Chamon C., Cugliandolo, L.F., Iguain, J.L., Kenett, M.P.: *Phys. Rev. B* **68**, 134442 (2003).
28. Jaubert, L.C., Chamon, C., Cugliandolo, L.F., Picco, M.: *J. Stat. Mech.* (2007) P05001.
29. Aron, C., Chamon, C., Cugliandolo, L.F., Picco, M.: *J. Stat. Mech.* P05016, (2008).
30. Ogielski, A.: *Phys. Rev. B* **32**, 7384 (1985).
31. Cruz, A., Pech J., Tarancón, A., Tellez, P., Ullod, C.L., Ungil C.: *Comp. Phys. Comm.* **133**, 165 (2001).
32. The Janus Collaboration: Belletti, F., Mantovani, F., Poli, G., Schifano, S.F., Tripiccione, R., Campos, I., Cruz, A., Navarro, D., Perez-Gaviro, S., Sciretti, D., Tarancón, A., Velasco, J.L., Tellez, P., Fernandez, L.A., Martin-Mayor, V., Muñoz Sudupe, A., Jimenez, S., Maiorano, A., Marinari, E., Ruiz-Lorenzo, J.J.: Computing in Science & Engineering **8**, 41-49 (2006); Belletti, F., Cotallo, M., Cruz, A., Fernandez, L.A., Gordillo, A., Maiorano, A., Mantovani, F., Marinari, E., Martin-Mayor, V., Muñoz Sudupe, A., Navarro, D., Perez-Gaviro, S., Ruiz-Lorenzo, J.J., Schifano, S.F., Sciretti, D., Tarancón, A., Tripiccione, R., Velasco, J.L.: *Comp. Phys. Comm.* **178**, 208 (2008); Belletti, F., Cotallo, M., Cruz, A., Fernandez, L.A., Gordillo, A., Guidetti, M., Maiorano, A., Mantovani, F., Marinari, E., Martin-Mayor, V., Muñoz Sudupe, A., Navarro, D., Parisi, G., Perez-Gaviro, S., Rossi, M., Ruiz-Lorenzo, J.J., Schifano, S.F., Sciretti, D., Tarancón, A., Tripiccione, R., Velasco, J.L.: preprint arXiv:0710.3535.
33. The Janus Collaboration: Belletti, F., Cotallo, M., Cruz, A., Fernandez, L.A., Gordillo-Guerrero, A., Guidetti, M., Maiorano, A., Mantovani, F., Marinari, E., Martin-Mayor, V., Muñoz Sudupe, A., Navarro, D., Parisi, G., Perez-Gaviro, S., Ruiz-Lorenzo, J.J., Schifano, S.F., Sciretti, D., Tarancón, A., Tripiccione, R., Velasco, J.L., Yllanes D.: *Phys. Rev. Lett.* **101**, 157201 (2008).
34. Cooper, F., Freedman, B., Preston, D.: *Nucl. Phys. B* **210**, 210 (1982).
35. Caracciolo, S., Edwards, R.G., Ferreira, S.J., Pelissetto, A., Sokal, A.D.: *Phys. Rev. Lett.* **74**, 2969 (1995).
36. Ballesteros, H.G., Fernandez, L.A., Martin-Mayor, V., Muñoz Sudupe, A.: *Phys. Lett. B* **378**, 207 (1996); *Phys. Lett. B* **387**, 125 (1996); *Nucl. Phys. B* **483**, (1997) 707.
37. Lee, L.W., Young, A.P.: *Phys. Rev. Lett.* **90**, 227203 (2003); Campos, I., Cotallo-Aban, M., Martin-Mayor, V., Perez-Gaviro, S., Tarancón, A.: *Phys. Rev. Lett.* **97**, 217204 (2006).
38. Amit, D.J., Martin-Mayor, V.: Field Theory, the Renormalization Group and Critical Phenomena, World-Scientific, Singapore, third edition (2005).
39. Hasenbusch, M., Pelissetto, A., Vicari, E.: *J. Stat. Mech.* L02001 (2008); preprint arXiv:0809.3329 (2008).
40. Toulouse, G.: *Communications on Physics* **2**, 115 (1977).
41. Marinari, E., Parisi, G.: *Phys. Rev. Lett.* **86**, 3887 (2001).
42. See e.g. Berthier, L., Biroli, G., Bouchaud, J.-P., Cipelletti, L., El Masri, D., L'Hôte, D., Ladieu, F., Pierno, M.: *Science* **310**, 1797 (2005) and references therein.
43. See e.g. Sokal, A.D.: Monte Carlo Methods in Statistical Mechanics: Foundations and New Algorithms. In DeWitt-Morette, C., Cartier, P., Folacci, A. (eds.) Functional Integration: Basics and Applications (1996 Cargèse school), Plenum, N.Y., (1997).
44. Frigo, M. and Johnson, S.G.: Proceedings of the IEEE **93**, 216 (2005).
45. Parisi, G., Ranieri, P., Ricci-Tersenghi, F., Ruiz-Lorenzo, J.J.: *J. Phys. A: Math. Gen.* **30**, 7115 (1997)
46. Franz, S., Parisi, G., Virasoro, M.: *J. Phys. I (France)* **4**, 1657 (1994).
47. Parisi, G., Ricci-Tersenghi, F., Ruiz-Lorenzo, J.J.: *Phys. Rev. E* **60**, 5198 (1999).
48. Marinari, E., Parisi, G., Ruiz-Lorenzo, J.J., Ritort, F.: *Phys. Rev. Lett.* **76**, 843 (1996).
49. Granberg, P., Svedlindh, P., Nordblad, P., Lundgren, L., Chen, H.S.: *Phys. Rev. B* **35**, 2075 (1987).
50. Préjean, J.J., Souletie, J.: *Phys. Rev. B* **37**, 577 (1988) and references therein.

-
51. Parisi, G., Ranieri, P., Ricci-Tersenghi, F., Ruiz-Lorenzo, J.J.: *J. Phys. A.: Math. Gen.* **30**, 7115 (1997).
 52. Contucci, P., Giardina, C., Giberti, C., Parisi, G., Vernia, C.: *Phys. Rev. Lett.* **99**, 057206 (2007); Contucci, P., Giardina, C., Giberti, C., Vernia, C.: *Phys. Rev. Lett.* **96**, 217204 (2006).
 53. Bray, A.J.: *Adv. Phys.* **43**, 357 (1994).
 54. Cugliandolo, L.F., Kurchan, J., Parisi, G.: *J. Phys. (France)* **4**, 1641 (1994).
 55. Palassini, M., Liers, F., Juenger, M., Young, A.P.: *Phys. Rev. B* **68**, 064413 (2003).
 56. Schehr, G., Rieger, H.: *Phys. Rev. B* **71**, 184202 (2005); Castillo, H., Le Doussal, P.: *Phys. Rev. Lett.* **86**, 4859 (2001).
 57. Marinari, E., Parisi, G., Rossetti, D.: *Eur. Phys. J. B* **2**, 495 (1998).
 58. Dupuis, V., Vincent, E., Bouchaud, J.-P., Hammann, J., Ito, A., Aruga Katori, A.: *Phys. Rev. B* **64**, 174204 (2001).